

Injury Risk Assessment of the Femur in Children with Osteogenesis Imperfecta

Jessica Marie Fritz
Marquette University

Recommended Citation

Fritz, Jessica Marie, "Injury Risk Assessment of the Femur in Children with Osteogenesis Imperfecta" (2016). *Dissertations (2009 -)*. Paper 645.
http://epublications.marquette.edu/dissertations_mu/645

INJURY RISK ASSESSMENT OF THE FEMUR IN CHILDREN
WITH OSTEOGENESIS IMPERFECTA

by

Jessica M. Fritz, M.S.

A Dissertation submitted to the Faculty of the Graduate School,
Marquette University,
in Partial Fulfillment of the Requirements for
the Degree of Doctor of Philosophy

Milwaukee, Wisconsin

May 2016

ABSTRACT
INJURY RISK ASSESSMENT OF THE FEMUR IN CHILDREN
WITH OSTEOGENESIS IMPERFECTA

Jessica M. Fritz, M.S.

Marquette University, 2016

Osteogenesis imperfecta (OI) is a genetic disorder characterized by increased bone fragility and decreased bone mass, which leads to high rates of bone fracture. OI has a prevalence of 1/5,000 to 1/10,000 in the United States. About 90% of persons with OI have a genetic mutation in the coding for collagen type I, which is the major protein of connective tissues, including bone. While its prevalence classifies it as a rare disease, it is the most common disorder of bone etiology. Until recently, little was known about the mechanics and materials of OI bone or their impact on fracture risk. Fracture risk is typically characterized by clinical type and radiographs. Finite element (FE) models have recently been developed to examine fracture risk during ambulation and various daily activities of the femur and tibia in children and adolescents with OI.

This research aims to provide further information about the impact of OI in children and adolescents during loading conditions. FE models of the femur with normal bone, OI type I (mild) bone and OI type III (severe) bone material properties were developed and analyzed. These models showed the effects of lateral bowing versus increased gluteus medius and gluteus maximus force production on bone injury risk. Lateral bowing and muscle force increase permutations to the standard model of no bowing and normal muscle forces during ambulation showed significant changes to stress levels. Along with FE models, quantitative gait analyses were performed on 10 children with mild OI and ten age- and gender-matched controls to analyze the firing patterns of the gluteus medius and gluteus maximus muscles during normal ambulation. The OI population exhibited a delay in gluteus maximus activation. Additional FE models examined the impact of creating the model directly from a CT scan of a child with severe OI versus scaling a standard model to match the size and shape of an OI femur based on x-ray images alone. Comparison of these two model geometry development techniques resulted in a significant difference in femoral stresses and strains.

ACKNOWLEDGEMENTS

Jessica M. Fritz, M.S.

First and foremost, I would like to thank my friends and family who have supported and loved me throughout my life and, most recently, during my dissertation journey. I would like to extend particular gratitude to my mother, Julane, who is one of my best friends and has always been my biggest supporter.

I would also like to thank the Marquette University community for my graduate education and employment since 2005. The environment at Marquette University has provided a wonderful place for me to grow personally and professionally. I am especially grateful to my dissertation committee members for their kindness, teaching, guidance and mentorship through my education and career. Lastly, I would like to especially thank my boss and dissertation director, Dr. Gerald Harris. His impact on my life has extended beyond these pages and has helped me discover and pursue my career passion.

TABLE OF CONTENTS

ACKNOWLEDGEMENTS.....	i
LIST OF TABLES.....	iv
LIST OF FIGURES.....	v
CHAPTER	
1. Introduction.....	1
1.1. Background.....	3
1.1.1. Osteogenesis Imperfecta (OI).....	3
1.1.2. Finite Element Analysis (FEA).....	11
1.1.3. Patient-Specific Modeling Parameters.....	18
1.2. Specific Aims.....	21
2. Loading Effects: Geometry versus Intrinsic Forces.....	24
2.1. Background.....	24
2.2. Methods.....	24
2.2.1. Model Development.....	24
2.2.2. Analysis.....	26
2.3. Results.....	30
2.4. Discussion.....	35
3. Muscle Firing Pattern Variations between a Population with OI Type I and an Age- and Gender-Matched Control Population.....	41
3.1. Background.....	41
3.2. Methods.....	42
3.2.1. Data Collection.....	42

3.2.2. Analysis.....	45
3.3. Results.....	49
3.4. Discussion.....	52
4. Analysis of Model Geometry Development: Individual Computed Tomography (CT) Scan versus Biplanar X-ray Scaling	56
4.1. Background.....	56
4.2. Methods.....	56
4.2.1. Model Development.....	56
4.2.2. Analysis.....	62
4.3. Results.....	62
4.4. Discussion.....	63
5. Conclusion	67
5.1. Study Motivation	67
5.2. Summary of Findings.....	70
5.3. Limitations and Future Directions	73
Bibliography	78

LIST OF TABLES

Table 2.1 Material properties of the femoral finite element models	25
Table 2.2 Muscle loading forces as a percentage of body weight in Newtons (%BW in N).....	29
Table 2.3 Maximum principal stress levels (MPa)	30
Table 2.4 Maximum principal stress increases (%)	31
Table 2.5 Injury risk (IR) values for normal pediatric bone	32
Table 2.6 Injury risk (IR) values for OI type I pediatric bone	32
Table 2.7 Injury risk (IR) values for OI type III pediatric bone.....	32
Table 2.8 Percent increases of IR for normal pediatric bone	33
Table 2.9 Percent increases of IR for OI type I pediatric bone	33
Table 2.10 Percent increases for OI type III pediatric bone.....	34
Table 2.11 Results of statistical analysis of maximum principals stress values between bone types.....	35
Table 2.12 Results of statistical analysis of injury risk (IR) values between bone types	35
Table 3.1 Marker set used for gait analysis.....	44
Table 3.2 Temporal spatial gait parameters comparison between control and osteogenesis imperfecta type I (OI) populations.....	50
Table 3.3 Gluteus medius EMG timing comparison between sides	51
Table 3.4 Gluteus maximus EMG timing comparison between sides	51
Table 3.5 Gluteus medius and gluteus maximus EMG timing comparison between control and osteogenesis imperfecta type I (OI) populations	52
Table 4.1 Material property assignments for femoral diaphysis models	57
Table 4.2 Results of femoral diaphysis models.....	63

LIST OF FIGURES

Figure 1.1 A child with mild/moderate OI and right femur deformity next to three femur models depicting deformity commonly seen in OI	4
Figure 2.1 Proximal end of the finite element (FE) model of a femur with cortical (green) and cancellous (red) bone sections	26
Figure 2.2 FE femoral model with muscle loads (yellow), boundary conditions on the condyles (blue) and applied gait kinetics on the femoral head and midcondylar nodes (gray)	27
Figure 2.3 Models of the femur with (a) no bowing, (b) 5 mm lateral bowing and (c) 15 mm lateral bowing	28
Figure 2.4 Contour plots of maximum principal stress distribution and levels (red = high, blue = low).....	34
Figure 3.1 The Motion Analysis Laboratory at Shriners Hospitals for Children – Chicago	42
Figure 3.2 Instrumented motion analysis subjects	43
Figure 3.3 Representative control population EMG data	47
Figure 3.4 Representative OI population EMG data.....	48
Figure 3.5 The right glutueus maximus plot of one subject.....	49
Figure 4.1 A coronal plane slice of the CT of the right femur.....	57
Figure 4.2 Three stages of femur segmentation in Seg3D from CT scan of a pediatric patient with OI type III.....	58
Figure 4.3 Volumetric rendering of OI femur from CT scan in Seg3D.....	58
Figure 4.4 3D solid models of a pediatric femur with OI type III (left) and a normal adult femur (right).....	59
Figure 4.5 Solid model of the diaphysis of the CT femur.....	59
Figure 4.6 Building block structure for the CT femur model in IA-FEMesh.....	60
Figure 4.7 Mesh of the CT femur diaphysis	60

Figure 4.8 Local coordinate system for the CT femur model.....	60
Figure 4.9 Solid model of the scaled femur diaphysis.....	61
Figure 4.10 Building block structure for the scaled femur model in IA- FEMesh.....	61
Figure 4.11 Mesh of scaled femoral diaphysis	61
Figure 4.12 Contour plots of the maximum principal stresses for the CT (left) and scaled (right) models	63

1. Introduction

Osteogenesis imperfecta (OI) is a genetic disorder characterized by increased bone fragility and decreased bone mass, which leads to high long bone fracture rates. About 90% of persons with OI have a mutation in the genes that code for collagen type I – the major protein of bone [1]. It is estimated that OI affects between 20,000 and 50,000 people in the United States [2]. At least 15 types of OI have been documented to date, with type I being the mildest form, type IV being a moderate form and type III being the most severe form that is compatible with life [3]. There are varying degrees of functional severity ranging from those who are able to ambulate independently without an assistive device to those who require a wheelchair for mobility. Severe OI is orthopaedically characterized by osteopenia, frequent fracture, progressive deformity, loss of mobility and chronic bone pain. Persons with severe OI often experience fractures during activities of daily living throughout their lifetime. As OI type I is the mildest form of the disorder, most persons with this type are ambulatory, but still have a higher than normal risk of experiencing fractures. However, the mechanisms behind the inherent bone fragility of OI remain loosely understood [4]. Current literature theorizes that the impaired collagen network with potentially low tensile strength and abnormal mineralization seen in OI bones affects its mechanical properties and may lead to the brittleness of OI bones [1, 2]. OI leads to bones with low trabecular bone mineral density (BMD), thin cortices and small and slender geometry. With limited data available on OI bone material properties, the roles of compromised material properties and abnormal bone geometry are unclear regarding the increased risk of fractures in long bones for persons with OI.

Understanding the biomechanics of bones in persons with OI is a key component to advancing knowledge about the disease, optimizing treatment and quality of life, as well as injury prevention. However, it is often not feasible to study bone biomechanics *in vivo*. Thus, modeling has the potential to play a key role in understanding how OI bones respond to loading experienced during various activities, especially ambulation.

Biomechanical modeling can provide insight into bone fracture risks, such as type and location, from single applied loads or repetitive loading. One method for obtaining this information is via finite element analysis (FEA). Patient-specific finite element (FE) models have been an effective tool for both bone strain and fracture strength assessment [5, 6]. They are used alongside motion analysis for gait pathologies, rehabilitation and sports training. One important developing application is the use of FEA to predict fractures in OI [7, 8]. Fracture prediction in OI patients may lead to altered prescription of activities and improved physical therapy.

Numerous factors contribute to fractures in OI patients including, but not limited to: altered bone material properties, geometry (size and shape) and loading. Therefore, these are three key components for a predictive or risk assessment model of OI long bone fracture. Models are currently being developed to examine the fracture risk assessment and validity of FEA applied to the whole OI femur [7, 8]. Ideally, these analyses will allow the implementation of better patient-specific models for persons with OI which will provide quantitative guidelines for activity limitations and rehabilitation or strengthening protocols to increase function and reduce fracture risk [9].

Across all types of OI, poor bone quality poses major orthopaedic and rehabilitation challenges. All treatments are performed with the goal of maximizing

function, minimizing deformity, maintaining patient comfort and allowing for independent living. Treatment strategies are generally personalized by clinicians based on motor function, functional needs and fracture risk. These assessments may include radiographs to examine bone morphology and bone density, outcomes questionnaires and clinical gait analysis. However, fracture risk is difficult to evaluate and is not quantitatively assessed in the clinical environment. FE models have the capability to assess stress and strain distributions of bones and, indirectly, the injury or fracture risk of loaded long bones. However, assessing fracture or injury risk using FE models requires some a priori knowledge on the stress levels that the modeled bone can withstand. This information can provide clinicians with a quantitative measure by which activities, treatment and rehabilitation/strengthening strategies can be prescribed.

1.1. Background

1.1.1. Osteogenesis Imperfecta (OI)

Osteogenesis imperfecta (OI) was first described in a thesis of a fragile-bone family by Ekman in 1788. Since then the nomenclature, classification and pathogenesis of brittle bone syndrome have evolved to what is commonly known as OI [10]. A prevalence of 1/5,000 to 1/10,000 in the United States has been suggested by Byers and Steiner [11]. While its overall prevalence classifies it as a rare disease, OI is the most common disorder of bone etiology [12]. Until relatively recently, OI was classified into types I-IV following the Silience classification scheme and was thought to solely be caused by either inadequate collagen production or poor collagen quality due to autosomal dominant mutations of the COL1A1 and COL1A2 genes that encode for type I

procollagens [13-15]. Sillence classification is based on phenotypic features, radiologic appearance of long bones and the mode of inheritance and is still the most widely used [3, 15]. The classification and phenotyping of OI is currently in a dynamic state as more genetic analyses are being formed and expanding the understanding of the disorder.

As of 2014, there were 15 known types of OI [3]. Several types were classified through histomorphometric studies and linkage analyses and were defined from children previously classified with OI type IV [13]. Genetic analyses have shown that only types I-IV may be linked to mutations in COL1A1 or COL1A2; though only types I and IV are not caused by any other genetic mutation and are always autosomal dominant [3]. OI type I is classified as mild or non-deforming and phenotype presentation includes a short or normal stature, blue sclera and mild joint laxity (Figure 1.1) [3, 14]. Type III is the most severe form of OI that is compatible with life, as type II is a perinatal lethal form of the disease, and presents as a severe, deforming disorder with phenotype presentation of white or blue sclera, dentinogenesis imperfecta (DI), short stature, severe scoliosis and wheelchair dependence [3, 14]. OI type IV is classified as a moderately deforming disorder with phenotypic presentation of moderate skeletal deformity, frequent use of aids for ambulation, blue sclera early that lighten with age, scoliosis and DI [3, 14]. Types V-XV are more variable in phenotype with types VII and

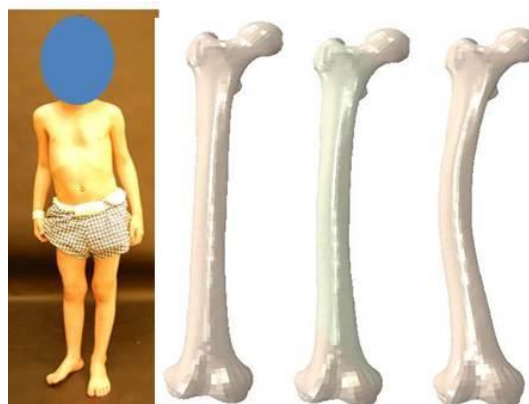


Figure 1.1 A child with mild/moderate OI and right femur deformity next to three femur models depicting deformity commonly seen in OI. Left model: no lateral bowing. Middle model: 5 mm/10° of lateral bowing. Right model: 15 mm/30° of lateral bowing.

VIII being specific to First Nations Quebec families and the South African black families, respectively [3]. New types are still being defined and characterized as genetic analyses expand. To date, osteoblast dysfunction is the common denominator across OI types [12]. In the simplest terms, osteoblasts are the cells that make bone. They form the extracellular matrix that becomes mineralized bone. Thus, osteoblast dysfunction leads to abnormal bone tissues. The functional deficit of osteoblast cells in OI affects both bone modeling and remodeling. Bone modeling is responsible for the growth in width of bone while bone remodeling is controls bone tissue renewal to prevent the accumulation of tissue damage [12]. Interruptions or alterations to this process would result in abnormal bone formation. Osteoblast dysfunction could cause bones that are smaller and more slender than normal as well as uneven and abnormal geometry.

OI types I and IV are the most common forms that allow for independent ambulation. These two types of OI have a characteristic increased risk of bone fracture due to their genetic mutation directly affecting the primary protein of bone formation. While the mutation responsible for type I affects the amount of collagen present in bones, the mutations of type IV affect the quality of collagen and thus the bone quality [3, 14]. This heterogeneous group of disorders affecting bone quality and geometry presents orthopaedic treatment requirements and challenges.

Persons with OI often have bones with low mass and decreased mechanical strength, which can lead to frequent fractures, progressive long bone deformity and growth deficiency. The severity of the disorder is clinically diverse and markedly influences the longevity and function of persons with OI. Compared to the bones of children without OI, those of children with the disorder exhibit fewer and thinner

trabeculae as well as reduced cortical width [15]. The low bone mass of OI is evident in its low mineral density and diminished material distribution. Both of these lead to higher bone stresses in OI long from the same loads, such as body weight, being distributed over less material [4]. A histomorphometry study on iliac biopsies from 70 children with OI types I, IV and III between ages 1.5 and 13.5 years showed that the external size of the biopsy core did not change with age and that cortical width of the biopsies was generally well below normal [12]. These results indicate a bone modeling deficit in OI. This defect contributes to reduced bone strength in OI due to smaller cross sections and reduced cortical thickness of long bones compared to unimpaired bones [12]. Additionally, mechanical testing and micro-computed tomography (μ -CT) of OI diaphyseal bone specimens showed that decreased mechanical strength is associated with high intracortical vascular porosity within OI long bones [4, 16].

Current goals of orthopaedic treatment focus on reducing the amount of fractures a child with OI experiences, correcting/lessening long bone deformity and enhancing function and independence. More recently, reduction of fracture incidence and long bone deformity have received focus with a multidisciplinary team approach that includes the use of bisphosphonates, physical therapy and intramedullary rodding of the long bones [15]. Each of these strategies has the ultimate goal of improving the quality of life of persons with OI through fracture reduction and increased mobility.

Fracture risk of OI bones is often assessed based on phenotype of the disorder and the appearance of the long bones on clinical radiographs. Medical management of OI typically includes bisphosphonate therapy which inhibits bone resorption by osteoclasts. Intravenous (IV) pamidronate is the most commonly used bisphosphonate for OI

treatment. Outcomes on the bones of children with OI associated with IV pamidronate treatments compared with historical controls include reduced bone pain, improved bone mass of long bones and vertebrae as well as decreased fracture rates [15]. In 2006, Rauch et al. reported on the effects of long-term pamidronate treatment in children with OI. They found an 88% increase in cortical width of long bones and a 46% increase in cancellous bone volume [17]. Pamidronate administered via IV has been shown to increase cortical thickness and the number of trabeculae, but does not alter the thickness of trabeculae. It works by inhibiting bone resorption at the endosteal surface without interfering with bone formation at the periosteal surface [15]. Studies on the effects of oral bisphosphonates have shown mixed results, however. While one study showed fracture reduction after one year of oral alendronate therapy, two other studies showed no evidence of fracture reduction from oral risedronate therapy [15]. Bisphosphonates are one of the most-studied groups of medications and have a good overall safety profile with benefits far outweighing negative effects. This is credited to their specific targeting to bone tissue for osteoclastic inhibition, with very little of the drug being absorbed by the kidney, spleen and liver. There are, however, concerns of long-term exposure to oral bisphosphonates increasing the risk of esophageal cancer. There has also been a report of eye-related inflammatory complications affecting less than 1% of patients. There have been reports of subtrochanteric atypical femur fractures in those treated with oral bisphosphonates, however; these types of fractures have also been reported in other patient groups and in children with OI who are not undergoing bisphosphonate treatment [18].

Surgical management is commonly applied in young children with severe forms of OI. In these children, disuse osteopenia and residual deformity often follow fracture

immobilization and increase the risk of subsequent fracture and deformity. This leads to a cycle of refracture, immobilization and further deformity, which can only be stopped by surgical intervention [15]. In severe forms of OI, the upper extremity long bones frequently have progressive deformity. However, the upper extremities usually function well and do not require operative correction unless deformity is interfering with function and mobility or frequently fracture. Operative treatment of long bone deformity is commonly done in the long bones of the lower extremities [15].

While it is generally agreed upon that surgical management of intramedullary rodding of the long bones can reduce the incidence of fractures in children with OI, there is not general agreement regarding at what age it is optimum to begin operative lower extremity long bone stabilization [15]. The traditional approach towards deformity resulting from closed treatment of fractures at an early age has been to wait until the child reached 5 years of age to perform a corrective osteotomy [19]. The basis of this approach was to minimize operations on the lower extremity long bones as the child continues to grow [15]. In contrast, some have previously argued for the use of intramedullary nails before a child with severe OI is able to stand. They contended that the benefits of correction the deformity and the child having fewer and less painful fractures outweighs the risks of revision surgeries. However, use of bisphosphonates for medical management of severe OI may decrease the number of operative interventions required in this population [15].

A recent trend in surgical management in OI has moved towards intervening earlier in the child's life rather than later. It has been suggested that lower extremity intervention as early as when the child begins to pull up to stand will lead to improved

gross motor development, self-care and mobility [15]. Zeitlin et al. observed that infants with OI who are routinely treated with pamidronate show more rapid motor development. In these patients, surgery has been performed around the age of 18 months [20]. Some have suggested that early intervention will allow children with OI who were previously non-ambulatory to be able to walk. In contrast, others have argued that the severity of involvement of the disorder is more important than surgery when determining the probability of a child with OI being ambulatory [15].

Ambulatory ability is one consideration for surgical intervention of the lower extremities. For the femur in particular, one general guideline for surgical correction of deformity is an angle of 20° or greater [21]. While this is quantitative measure in itself, it is based on qualitative data and experience rather than quantitative assessment of the loading mechanics of OI bone. Quantitative analyses through FE modeling of *in vivo* loading have the potential to help determine the ambulatory potential of children with OI. The optimal analysis of femoral fracture risk would be patient-specific for each case. This would consist of a model of each OI femur with its geometry and the accompanying reduced mechanical strength of the bone as well as the external and intrinsic loading being applied to the bone during a modeled activity such as ambulation.

Compared with normal bone, little is known about the mechanical responses of OI bones. Until recently, all testing to determine OI bone material properties had indicated that it was an isotropic material rather than anisotropic like normal bone [14, 22-25]. Original nanoindentation testing on OI bone did not include specimens from patients with type I, which is the most common form of the disorder [22-24]. Thus, the original FE model of an OI type I femur had to approximate Young's modulus (E) based on data

from type IV bone specimens that had an average Young's modulus value of 19.19 GPa. This testing had produced an average Young's modulus for type III bone of 19.67 GPa [24]. Based on the data available at the time, the OI type I femur was modeled with a Young's modulus of 19 GPa [14]. In 2013, Albert et al. reported results from nanoindentation of OI bone specimens that included OI type I femoral bone. Their testing indicated that $E = 17.53$ GPa in OI type I interstitial femoral bone. This work was the first database of OI bone properties from nanoindentation that included results from type I specimens [25].

In 2012, Albert et al. designed and developed a mechanical testing methodology to machine and test miniature bone specimens as small as 5mm in length. This led to the first flexural strength testing results of OI bone through three-point bending [26]. The innovative methodology led to the machining of 59 samples of twelve diaphyseal long bone specimens from nine donors with OI types I, III and IV by Albert and colleagues [16]. Each sample was 5-6 mm in length, 0.7 mm in depth and 1 mm in width. These samples were machined in both the longitudinal and transverse directions [16]. All of these samples underwent three-point bending analysis based on the established methodology for testing miniature bone samples [16, 26]. The flexural testing provided information on maximum flexural strength ($\sigma_{f,max}$), Young's modulus (E) and flexural yield strength ($\sigma_{f,y}$). The longitudinally oriented specimen average results were: $E = 4.4$ GPa, $\sigma_{f,y} = 61.4$ MPa and $\sigma_{f,max} = 83.0$ MPa. The average results for the transverse specimens were: $E = 1.6$ GPa, $\sigma_{f,y} = 20.8$ MPa and $\sigma_{f,max} = 26.5$ MPa. These results showed a significant difference between properties in the longitudinal and transverse

directions [16]. This contradicts previous data from nanoindentation that had indicated OI bone exhibited isotropic material behavior [14, 22-24].

In conjunction with the flexural testing of the miniature OI bone beams, 21 of these samples were imaged by synchrotron micro-computed tomography (SR- μ CT) to determine vascular porosity, volumetric mineral density and osteocyte lacunar density [16]. These parameters did not differ significantly between the longitudinal and transverse samples. Average results from SR- μ CT scanning demonstrated a vascular porosity of 23.97%, an osteocyte lacunar density of 44,971 mm⁻³ and a volumetric tissue mineral density of 1.67 g/cm³ [16]. The vascular porosity of the OI bone samples was much higher than the values of 3-6% typically reported for the long bones of children and young adults. The elevated porosity in OI bone samples showed a strong, negative correlation with their material properties. This indicated that the fragility of OI bone may be partly attributed to the increased level of vascular pores in the diaphyseal cortex [16].

The increasing information on material and mechanical properties of OI bone not only increases understanding of the disorder, but provides valuable insight on its macrostructure. This data is imperative to develop accurate FE models of OI long bones to assess their response to loading and assess fracture risk.

1.1.2. Finite Element Analysis (FEA)

Finite element analysis (FEA), also called the finite element method (FEM), is an established computationally intensive numerical method commonly used to solve engineering and physics problems such as material response to loads, pressures, temperature, fluid flow, displacements, contacts, etc. [27]. Development of FEM dates back to structural engineering of aircrafts in the 1940s with one-dimensional line

elements. Two-dimensional analyses did not present until 1956, though the term *finite element* was not coined until 1960 [27, 28]. Since its development, advances in computing have allowed broad use of FEA throughout engineering disciplines and levels.

The FEM discretizes structures into a mesh of small elements. A series of differential equations are assessed at the vertices (nodes) of each element to provide a piecewise analysis of the structure's response to various conditions. FEA has become a reliable method for mechanical analysis of materials, especially in applications of fatigue testing and failure analysis. It can be used to simulate cyclic loading to failure in significantly shorter time. Benefits to using FEA include: increased accuracy, enhanced design and improved insight into critical design parameters, virtual prototyping, fewer hardware prototypes required, a faster and less expensive design cycle and increased productivity [29]. FEM can also be useful in flow dynamics analysis, thermal effects, molecular level analysis and crack propagation [30, 31]. A valid finite element (FE) model can significantly shorten the time for new product or process development and allow testing that could not otherwise be completed.

In 1972, FEA was introduced into the then relatively new field of biomechanics by Brekelmans and colleagues and has since become widely used in orthopaedic biomechanics [32]. Brekelmans et al. used FEA to investigate the stresses experienced by human bones under physiologic loading conditions [33]. This work demonstrated the ability for computational models to provide *in vivo* data without invasive means or cadaver testing. While FEA often substitutes for invasive or cadaver testing, the models are generally validated by experimental methods. The field of orthopaedic biomechanics has seen an increased use of FEA in the past 40 years. Applications include assessment of

bone strength for treatment recommendations and fracture risk analysis, fracture prediction, development of bone modeling scenarios, modeling of accident or trauma scenarios, and assessment of orthopaedic implants and devices [34-38]. In the early stages of FEA applications in biomechanics, it became clear that model accuracy relied on 3D bone geometry, bone material properties and the specific model loading conditions. Gupta et al. developed and validated a unique three-dimensional (3D) model of the human scapula using both the geometry and material property data available from computed tomography (CT) scan data. Unlike previous solid models in biomechanics, this scapula model used a combination of shell (2D) and solid (3D) elements, called a shell-solid mesh. The researchers assessed the accuracy of their model by comparing its surface stress and strain results to those obtained from experimental testing with strain gages mounted on fresh cadaveric scapulae [39]. There are multiple methods for mesh creation and their selection often depends on the origin of the model input data such as geometry and material properties as well their intended application.

Finite element models have been widely and effectively used to assess soft tissue, bone and orthopaedic material stresses and strains [33-36, 40-59]. Applications include orthodontics, pedestrian trauma simulations, device-bone interface, bone modeling, patient-specific fracture predictive models and more. One of the first studies of applying FEA to examine long bone fracture risk was performed in 2003 by Taddei and colleagues on femoral reconstructions in pediatric oncology patients. This model evaluated a proximal femur endoprosthesis in a child with Ewing sarcoma to determine fracture risk. The model's loading conditions were the hip joint reaction forces and abductor muscle forces. Taddei et al. assessed fracture risk by calculating the ratio between the bone tissue

strength and the predicted von Mises equivalent stress [60]. Since this study, many researchers have employed FEA to look at bone strength; however there are still no standard criteria for risk assessment in long bones. Bone fracture criteria that have been used include distortion energy, Hoffman and a strain-based Hoffman analogue (used for anisotropy), maximal normal stress, maximum normal strain, maximum shear strain, maximum shear stress, maximum normal strain, maximum shear strain, maximum shear stress, maximum principal stress, maximum principal strain, Cowin based on the Tsai-Wu model, Drucker-Prager stress Coulomb-Mohr and modified Mohr failure theories [14, 34]. The most appropriate theory often depends on the material being modeled and the analysis being performed. The von Mises stresses are often used as a criterion for isotropic materials [49] and maximum principals stresses are often used when examining fracture of brittle materials [61]. Many studies that look at femur fracture focus solely on the proximal femur and are focused on populations such as the elderly and those with osteoarthritis. Another femur fracture risk modeling application is in the field of trauma research. In this area, a validated lower-limb, non-linear 3D FEA model was developed to study the effects on the thigh of car-pedestrian impacts [62, 63]. While many early models did not account for muscle forces when examining bone strains or stresses to assess fracture risk, it is known that these forces can significantly alter the distribution of loads on the femur [14, 63-69]. Patient-specific predictive models have recently become common in orthopaedics. Some researchers have even called for patient-specific simulations through FEA as a necessity when determining the optimal device for orthopaedic procedures such as arthroplasty [59, 70]. Specifically for the femur, FEA is commonly applied to assess fracture risk at the hip (proximal femur) in patients with

osteoporosis. The majority of these models rely on CT scans to obtain 3D bone geometry. This type of modeling is known as CT/FEA studies. A review of CT/FEA for assessment of osteoporosis concluded that this methodology can accurately determine bone strength, fracture site, fracture risk and medication effects [34]. While CT/FEA has the capabilities to provide accurate 3D bone geometry as well as bone density distributions and properties, it comes with a larger radiation dose than other methods for obtaining this information.

The radiation of CT imaging makes it an infeasible option for examining children with OI as they typically undergo yearly dual x-ray absorptiometry (DXA) scans to assess BMD and have higher than normal rates of x-rays due to their increased fracture rates. The first application of FEA in OI was completed by Fritz et al. in 2007 [14]. A patient-specific model was developed to examine the fracture risk of a femur during normal ambulation of an adolescent female with OI type I from Shriners Hospitals for Children, Chicago (SHC-C) [14, 71]. This model's geometry originated from the standardized femur (SF) developed by Viceconti et al. [72]. Since the SF was developed from an adult male, the modeled patient's coronal plane x-rays were used to scale the femur to the appropriate geometry; this included size and mild lateral bowing equivalent to 5 mm beyond normal [14, 71]. Due to radiation and equipment restraints, single plane x-rays were the only available geometry reference. Ideally, CT images could provide not only specific geometries, but also material properties throughout the bone. However, the increased level of radiation from this modality makes them clinically uncommon and difficult to justify acquiring in the OI population which already receives several x-rays per year. The cost of magnetic resonance imaging (MRI) equipment and acquisition

obviated the feasibility of this modality for 3D image development on patients at SHC-C. Patient-specificity of the model was also included in the loading and boundary conditions of the FEA. This data originated from 3D gait analysis of the modeled subject at SHC-C. This analysis yielded the joint kinematics and kinetics of the lower body during ambulation at a self-selected speed. The dynamics data was input in the FE model as hip and knee forces and moments applied to the femoral head and condyles, respectively [14]. Unlike many FE models for fracture risk prediction or assessment, the model by Fritz et al. included loading conditions from forces due to activation of muscles attached to the femur [14, 71]. The OI femur was modeled as an isotropic material with a Young's modulus of 17 GPa and a Poisson's ratio of 0.3, as adapted from nanoindentation testing on OI bone specimens [14, 22-24, 71]. The importance of including muscle forces was published in 2009 by Fritz et al. who showed that maximum von Mises stresses in the FE model of the OI type I femur were sensitive to gluteus medius and gluteus maximum forces, but not to the other muscles attached to the femur and activated during ambulation [66]. Over the years, the femur model has evolved to have a hexahedral mesh instead of its original tetrahedral mesh [73]. It also has been modified to reflect the most recent mechanical property data. The more recent data from three-point bending analysis of specimens showed that OI bone is a transversely isotropic material with a cortical bone Young's modulus closer to 7 GPa than the 17 GPa reported from previous nanoindentation testing. With the material definition change, the fracture criterion was changed from von Mises stresses, which is applicable for isotropic materials, to maximum principal stresses [74].

Recently, Caouette et al. developed an FE model of OI tibiae for fracture risk assessment [75]. The tibia models employed principal strain criteria to assess fracture risk during two-legged hopping, lateral and torsional loading scenarios [4, 75]. Caouette and colleagues developed their models' geometry by combining 3D reconstructions from peripheral quantitative computed tomography (pQCT) and biplanar tibial x-rays mapped to a standardized 3D tibial model into a new 3D model for FEA. The material properties of the OI tibial models were based on nanoindentation data of cortical bone from OI type IV specimens or estimated based on bone apparent density measured from three different sites of the trabecular bone using pQCT [75]. Along with the femur and tibia models for long bone fracture risk assessment in OI, researchers have developed an FE humerus model [76, 77]. This model is important in OI due to the use of assistive devices and prior studies showing the potential for high humeral loads during crutch walking [76, 78]. A study of Lostrand crutch users showed a pediatric subject with cerebral palsy experienced joint reaction forces up to approximately 35% of their body weight. In this same study, a subject with OI had much lower maximum joint reaction forces at the elbow and should of approximately 15% of their body weight [78]. In 2011, Grover et al. reported that assisted ambulation can lead to a bending moment up to 24 Nm [79]. Further development of the FE humeral model and its applications during assisted ambulation in the OI population may be warranted. Orwoll et al. have also created an FE model with an OI application. While the other FE models with OI applications have been developed for pediatric fracture risk assessment, this model is used to estimate vertebral bone strength in adults with OI [76, 80]. FEA is a quantitative tool that is helping further the understanding of bone quality and guiding orthopaedic and rehabilitative treatment for

persons with OI. It provides a more complete assessment of the impacts of daily activities as well as functional strengthening protocols on bone strains and stresses.

1.1.3. Patient-Specific Modeling Parameters

Development of patient-specific FE models requires their inputs to come as directly from each patient as possible. These inputs include the model's geometry, material properties and loading applications.

Model geometry is obviously imperative to accurate assessment of stresses and strains resulting from applied loads. This is inherent in the definition of stress being the applied force over the area to which it is applied. In the case of analyzing femoral stresses during ambulation, the geometric size and shape of the femur are important factors.

Bowing of the femur in the lateral direction, as is commonly seen in OI, causes more of the bone to be away from the mechanical axis. This results in the compressive loading of the femur at the hip during ambulation which results in an increased bending moment, thus, increases the maximal stresses experienced by the lateral side of the bone [73, 81].

Along with overall bone shape differences, OI long bones exhibit further geometric variations from normal bones. Particularly in more severe forms of OI, long bones often have a narrow diaphysis and thin cortical bone shell compared to typical long bones [81]. Available data for geometric development of OI femurs is commonly restricted to planar x-rays that then must be matched to an existing 3D model of the bone. Ideally, computed tomography (CT) scans would provide an exact 3D model of each femur and its strength properties. The use of CT data to create 3D FE models has been in practice since the early 1990s [34]. However, due to their higher dose of radiation exposure and the increased incidence of scans taken of children with OI because of their fracture rate, CT

scans are not normally acquired in this population. Magnetic resonance imaging (MRI) scans could also be used to create a 3D model directly from a femur scan. While they do not subject the patient to ionizing radiation, MRI scans are expensive and have been used less extensively to image bone. Bone segmentation is often a challenge from MRI images due to poor resolution from clinical constraints and the heterogeneity of intensity from the cancellous and cortical bone areas [82].

Modeling of a material's response to loading relies on accurate property data. The inherent mineral and collagen abnormalities of OI alter the bone properties at the material level compared to normal, healthy bone [81]. Histomorphometric analyses have indicated that OI bone exhibits decreased cortical thickness and trabecular bone volume per tissue volume [25, 83]. Early material testing on human OI bone was performed by Fan et al. using nanoindentation techniques [22-24]. Nanoindentation measures the force required to press the tip of a diamond indenter into a material specimen, such as bone, as a function of indentation depth. As the name implies, this testing methodology is performed with nanometer resolution. These measurements are often used to evaluate the brittleness of a material, and thus, extrapolate properties such as Young's modulus and hardness [14]. Nanoindentation testing performed by Fan et al. on transverse and longitudinal specimens of both cortical and cancellous samples of OI bone indicated that there were no significant differences across directions, which indicates an isotropic material and is contradictory to normal bone [22]. Normal bone is classified as anisotropic with directionally independent material properties. These original studies indicated that OI type I had a Young's modulus of approximately 19 gigapascals (GPa) and a Poisson's ratio of 0.3 [14]. In 2013, Albert et al. reported on the results of

nanindentation testing on a set of eleven OI pediatric bone specimens (six with type I, five with type III). Their results showed that OI type I had a Young's modulus around 18 GPa, which was 7% higher than the modulus observed in OI type III. The average modulus of OI type III was 13% higher than reported data for normal pediatric bone [25].

Adequately representing the *in vivo* response of bones to applied loads in FEM requires accurate modeling of the kinetics. This can be best accomplished through gait analysis, which provides joint forces and moments, when modeling loading during ambulation [14]. Jiang et al. recently published an FE model for hip fracture risk assessment using a general loading of 2.5 times body weight to mimic single limb support during gait and no muscle force contributions [43]. Other FEA fracture risk models have also used generalized forces rather than patient- or subject-specific data, which would provide more accuracy [84]. The necessity to include muscle forces in orthopaedic biomechanics FE models was recognized by Viceconti et al. releasing a new version of their standardized femur model for FEA that includes muscle attachment areas [69]. Clinical gait analysis traditionally uses inverse dynamics to calculate the forces and moments applied to each joint of the lower body while a person ambulates. However, these calculations neglect the contributions of muscle contractions to the loads experienced by the bones and joints of the lower body [14]. Traditional gait analysis includes electromyography (EMG) data from surface electrodes on four groups of muscles, bilaterally. These muscles include: 1) rectus femoris, 2) medial hamstring, 3) medial gastrocnemius, and 4) tibialis anterior. This provides activation timing data of these muscles throughout the gait cycle. However, this set does not include all the muscles that are active during ambulation and attach to the femur. A study of the

contribution to femoral bone strain during gait from muscular contractile forces showed that the gluteus medius and gluteus maximus have obvious impacts [66]. The original femur FE model during OI type I ambulation included patient-specific kinetics from gait analysis and muscle activation patterns from the synchronized EMG [14, 71]. However, this gait data and the subsequent model did not include patient-specific data on the gluteus muscles. Their force data timing was based on normal activation patterns. Graf et al. have previously shown that children with OI type I do not exhibit normal gait. Their population of children with OI type I spent more time in the stance phase of gait and exhibited longer double limb support than their age-matched peers without OI [85]. Altered gait timing may affect gait kinetics and the timing of muscle activations. Graf et al. also showed significant delays in the timing of peak hip extension, peak knee extension and peak knee flexion in the OI population [85]. To date, nobody has reported on altered muscle activation patterns during ambulation in children with OI, especially in the gluteus medius and gluteus maximus muscles. These muscles deserve further examination because they attach to the proximal femur. Their activation forces have been shown to have a strong impact on femoral stresses during gait [66]. The chosen approach of using patient-specific loads from gait analysis provides for a more accurate input data set than using generalized forces normalized to body weight as temporal and kinematic parameters of ambulation can affect gait kinetics and muscles forces applied to the model.

1.2. Specific Aims

The specific aims of the project and their corresponding hypotheses were:

1. The effects of lateral bowing and femoral muscle loading on the FE model of a femur were examined. The loading condition modeled was representative of the joint reaction forces and the intrinsic muscle forces present during the mid-stance phase of gait. This is the phase of gait where the femur experiences the highest level of stress. The model was analyzed for a mild bowing of 10° and a significant bowing of 30° . Muscle forces were incrementally and individually increased at levels of 10%, 15% and 20% for the gluteus maximus and gluteus medius muscles.

Hypothesis: Increases in femoral maximum principal stress due to a bowing of 30° are significantly less than those due to a 10% increase in gluteal muscle contractile forces.

2. The differences between muscle activation patterns in ten children and adolescents with OI and ten age- and gender-matched peers were statistically assessed from data collected during gait analysis.

Hypothesis: Ambulatory children and adolescents with OI type I exhibit significantly different EMG timing patterns than age-matched controls.

3. Maximum principal stresses and maximum principal strains were evaluated and compared between two FE models of the femoral diaphysis of a young adult with OI type III. The two models had their geometry derived from different clinical scans. One model was based on a CT scan of the femur and the other was a 3D femur model of an adult femur that was scaled to the OI femur based on a coronal plane x-ray view of the OI patient's femur.

Hypothesis: Femoral stress results from an FE model of a young adult with OI are not significantly affected by the clinical imaging modality used to match patient-specific femur geometry (CT versus 3D model scaled from planar x-rays).

These studies aim to provide new, quantitative information on femoral stresses and fracture risk in OI. Research and clinical care in OI both have the goals of improving the lives of persons with the disorder and ultimately reducing fracture rates. Accurate patient-specific models require as many patient-specific inputs as possible. While not all parameters are feasible to obtain for each patient, this work aims to help establish methodology for FEA to assess femoral fracture in individual persons with OI.

2. Loading Effects: Geometry versus Intrinsic Forces

2.1. Background

Finite element models and analyses were used to test the hypothesis that increases in femoral maximum principal stress due to a bowing of 30° are significantly less than those due to a 10% increase in gluteal muscle contractile forces. Previous work on the sensitivity to intrinsic forces (from muscle activation forces) of the FE model of an OI femur showed that stresses are sensitive only to loading changes from the gluteus medius and gluteus maximus muscles [66]. Another prior preliminary study showed that resultant stresses have a positive linear correlation with increased lateral bowing of the OI femur model [73]. Clinically, a lateral bowing of 30° of the femur serves as a guideline for surgical correction [21]. While prior studies have been completed looking at the effects of lateral bowing and gluteal muscles forces, these parameters' effects were not compared. They cannot be compared to each as a review since they were performed on models that did not contain the same mesh and inputs.

2.2. Methods

2.2.1. Model Development

An existing OI femur 3D FE model was used for this study [71]. This model consists of 11,484 hexahedral elements of type C3D8 meshed in IA-FEMesh and eight shell elements of type S4 added in ABAQUS. The C3D8 elements are brick elements with eight nodes which comprise two element sets defined for the cortical and cancellous bone layers. This allows for the element sets to be assigned material properties respective

of their type of bone. The S4 shell elements are four-node planar elements applied to the estimated hip and knee joint centers of the femur. These locations correspond to where joint reaction forces and moments from gait analysis were calculated [14]. The shell elements are necessary to apply a moment to the FE model. The loading for the model (joint reaction forces and moments and intrinsic forces from muscle) was representative of the forces experienced by the femur of the originally modeled 12-year-old female with OI type I during the loading response phase of her normal ambulation [14].

Models were developed to represent the mechanical response of femurs of normal children as well as those with OI type I and OI type III. The material properties (Table 1) for these models were based on the results of three-point bending tests of bone specimens, literature and calculations [86].

Table 2.1 Material properties of the femoral finite element models. In the table, E is Young's modulus, ν is Poisson's ratio and G is shear modulus.

Bone Origin	Bone Type	Transverse			Longitudinal		
		E (GPa)	ν	G (GPa)	E (GPa)	ν	G (GPa)
<i>Normal</i>	<i>Cortical</i>	8.2	0.3	3.1	15.0	0.3	5.8
	<i>Cancellous</i>	4.9	0.2	2.1	9.0	0.2	3.8
<i>OI Type I</i>	<i>Cortical</i>	4.6	0.3	1.8	7.4	0.3	2.8
	<i>Cancellous</i>	2.8	0.2	1.2	4.4	0.2	1.9
<i>OI Type III</i>	<i>Cortical</i>	3.7	0.3	1.4	5.7	0.3	2.2
	<i>Cancellous</i>	2.2	0.2	0.9	3.4	0.2	1.4

The three-point bending tests provided Young's modulus (E) in both the longitudinal and transverse orientations of femoral diaphysis bone specimens. All specimens were from males who were 10-11 years old. All types of bone (normal and OI) were assigned the same Poisson's ratios (ν) of 0.2 and 0.3 for the cancellous and cortical

bone sections, respectively [86]. Based on the data available, shear modulus (G) was calculated according to Hooke's law (Eqn. 2.1):

$$G = \frac{E}{2(1-\nu)} \quad (2.1)$$

The variables in the equation were previously defined as: G is shear modulus, E is Young's modulus and ν is Poisson's ratio. The femurs were modeled as transversely isotropic, linear elastic materials. The cortical and cancellous material layers were assigned orientations with the same axes as the global coordinate systems (Figure 2.1).

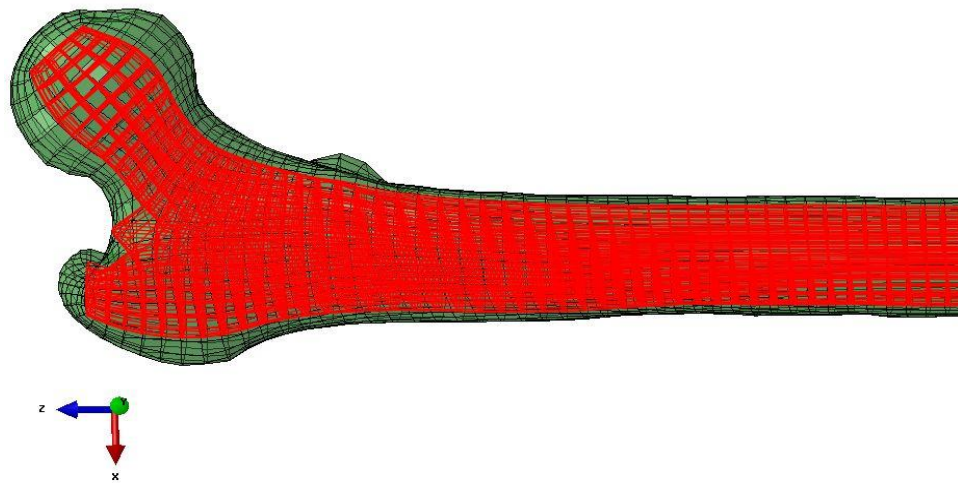


Figure 2.1 Proximal end of the finite element (FE) model of a femur with cortical (green) and cancellous (red) bone sections.

2.2.2. Analysis

First, the effects of femoral geometry on stresses and fracture risk were assessed. All femur models were the same length as the base FE OI femur model based on a 12-year-old female with OI type I. Each femur was loaded based on the same patient's femoral loads during the midstance of her normal ambulation and had boundary conditions of fixed femoral condyles in all six degrees of freedom (Figure 2.2) [14, 71].

Only the midstance phase of gait was modeled for this study as my prior work showed that this is the phase of gait associated with the highest femoral stresses [71]. The muscle loading areas were based on anatomical attachments on the femur. Forces were based on literature as a percentage of body weight with lines of action based on kinematics and relative angles to the adjoining bone's muscle attachment area [71]. The joint forces and moments, baseline muscle forces and the locations of loading and boundary conditions were the same for each model.

Each femur bone phenotype (normal, OI type I and OI type III) was modeled with three different diaphyseal curvatures: 1) normal, 2) 5 cm/10° and 3) 15 cm/30° of lateral bowing (Figure 2.3). The lateral bowing of the femur was completed by applying a displacement to a mid-diaphyseal set of nodes in on the model without bowing and writing those nodes back to the input file to create the smoothly curved geometries shown in Figure 2.3. This was accomplished through ABAQUS CAE (SIMULIA; Providence, Rhode Island).

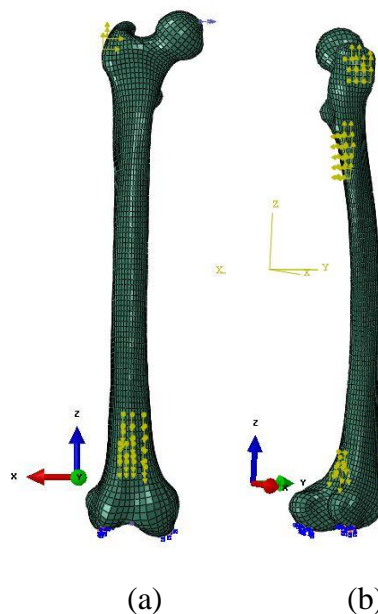


Figure 2.2 FE femoral model with muscle loads (yellow), boundary conditions on the condyles (blue) and applied gait kinetics on the femoral head and midcondylar nodes (gray). (a) anterior view and (b) lateral view to show all modeled muscle forces: gluteus medius, gluteus maximums, vasti, gastrocnemius (lateral and medial heads).

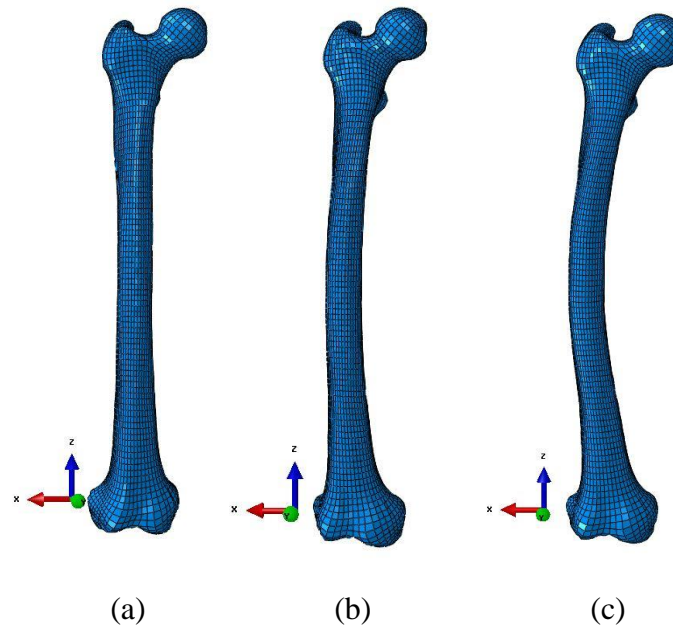


Figure 2.3 Models of the femur with (a) no bowing, (b) 5 mm lateral bowing and (c) 15 mm lateral bowing.

Following development of the nine geometrically varied models (three bone phenotypes times three bowing levels); six additional models were developed for each geometry variation to examine the effects of intrinsic loads from gluteal muscle forces. The six additional models held all other loading constant, but altered the loading as follows: 1) 10% increase in the gluteus medius, 2) 15% increase in the gluteus medius, 3) 20% increase in the gluteus medius, 4) 10% increase in the gluteus maximus, 5) 15% increase in the gluteus maximus and 6) 20% increase in the gluteus maximus forces (Table 2.2). These represent functional increases in muscle forces that would occur due to faster walking speeds, running, ascending and descending stairs, and isolated strengthening [87-89].

Table 2.2 Muscle loading forces as a percentage of body weight in Newtons (%BW in N). Gluteus medius = GMed. Gluteus maximus = GMax. Force increases are expressed as +10%, representing a 10% increase from baseline force levels [71].

Muscle Scenario	Muscle Force & Direction (%BW in N)			
	<i>Gluteus Medius</i>	<i>Gluteus Maximus</i>	<i>Vasti</i>	<i>Gastrocnemius</i>
Baseline	37.20	52.00	39.60	8.40
GMed +10%	40.92	52.00	39.60	8.40
GMed +15%	42.78	52.00	39.60	8.40
GMed +20%	44.60	52.00	39.60	8.40
GMax +10%	37.20	57.20	39.60	8.40
GMax +15%	37.20	59.80	39.60	8.40
GMax +20%	37.20	62.40	39.60	8.40

All models were run with a single loading step and each model's maximum principal stress was examined and recorded. Principal stress direction coincided with the longitudinal axis of the femur, so maximum principal stress was analyzed because it corresponded with the area of the femur at the highest risk for fracture under axial loading [71]. Yield stress was chosen as the critical value for femoral fracture risk since it represents the stress at which the bone would experience irreversible damage. Maximum principal stresses were compared to yield stress results from mechanical testing of the bone specimens used to establish model material properties [86]. A fracture risk assessment metric was established (Eqn. 2.2).

$$IR = \frac{\sigma_{mp}}{\sigma_y} \quad (2.2)$$

In Equation 2.2, IR is the bone injury risk level, σ_{mp} is maximum principal stress and σ_y is yield stress. Before the bone reaches a stress level causing yielding, the fracture risk level will be below one. An IR value above one would indicate the bone has reached a loading level that will cause irreversible damage. Each model was assessed for maximum principal stress and IR was calculated.

Analyses were performed on the results to determine if the increased loading from muscle forces had a higher impact on principal stresses than increased lateral bowing. This comparison was performed within each bone type by calling the model with no bowing and baseline muscle forces the standard. The IR (Eqn 2.2) of permutation model (bowing level or muscle force increase) was calculated as a percent increase from the standard IR value. The results between bone types were statistically assessed for significant differences in maximum principal stresses and IR values using Welch's t-test with a significance level set at $P > 0.05$.

2.3. Results

The results showed that incremental increases in muscle forces had a greater impact on femoral stresses than do increases in lateral bowing (Table 2.3). The femurs modeled with normal pediatric bone material properties experienced the greatest percent increases in maximal principal stresses followed by OI type I and OI type III bones, respectively (Table 2.4).

Table 2.3 Maximum principal stress levels (MPa).

<i>Normal Pediatric Bone</i>	Maximum Principal Stress (MPa)		
	No Bowing	5 mm Bowing	15 mm Bowing
Baseline Muscles	54.92	55.35	56.15
GMed +10%	56.47	57.45	57.02
GMed +15%	57.24	58.51	57.78
GMed +20%	58.01	59.57	59.61
GMax +10%	56.92	56.90	58.14
GMax +15%	58.00	57.75	59.14
GMax +20%	59.07	58.61	60.14
<i>OI Type I Bone</i>	Maximum Principal Stress (MPa)		
	No Bowing	5 mm Bowing	15 mm Bowing
Baseline Muscles	55.96	56.42	56.92
GMed +10%	57.37	58.34	58.83
GMed +15%	58.08	59.34	59.79
GMed +20%	58.77	60.34	60.74

Table 2.3 (Continued)

<i>OI Type I Bone</i>	Maximum Principal Stress (MPa)		
	No Bowing	No Bowing	No Bowing
GMax +10%	57.82	57.84	58.41
GMax +15%	58.82	58.55	59.57
GMax +20%	59.83	59.24	59.98
<i>OI Type III Bone</i>	Maximum Principal Stress (MPa)		
	No Bowing	5 mm Bowing	15 mm Bowing
Baseline Muscles	56.60	57.10	57.57
GMed +10%	57.99	58.85	59.24
GMed +15%	58.64	59.73	60.12
GMed +20%	59.2	60.67	61.02
GMax +10%	58.44	58.43	58.87
GMax +15%	59.34	59.08	59.51
GMax +20%	60.21	59.74	60.16

Table 2.4 Maximum principal stress increases (%). The increases were compared to the no bowing and baseline muscle forces model.

Parameter Change	Maximum Principal Stress Increase (%)		
	Bone Type		
	Normal Pediatric	OI Type I Pediatric	OI Type III Pediatric
5 mm Lateral Bowing Increase	0.78	0.82	0.88
15 mm Lateral Bowing Increase	2.24	1.72	1.71
25 mm Lateral Bowing Increase		3.06	2.65
10% Gluteus Medius Force Increase	2.82	2.52	2.46
15% Gluteus Medius Force Increase	4.22	3.79	3.60
20% Gluteus Medius Force Increase	5.63	5.02	4.59
10% Gluteus Maximus Force Increase	3.64	3.32	3.25
15% Gluteus Maximus Force Increase	5.61	5.11	4.84
20% Gluteus Maximus Force Increase	7.56	6.92	6.38

Increasing lateral bowing and muscle forces increased the risk of irreversible femoral bone injury as the IR approached a value of one. As expected, the IR values were low in the models of normal pediatric bone, higher in the models of OI type I bone and highest in models of OI type III bone (Tables 2.5-2.7).

Table 2.5 Injury risk (IR) values for normal pediatric bone. Risk increases as value approaches 1. GMed = gluteus medius; GMax = gluteus maximus. Increases in muscle activation levels are from the baseline “normal” level.

Bowing	Muscle Activation Level						
	Normal	GMed +10%	GMed +15%	GMed +20%	GMax +10%	GMax +15%	GMax +20%
0 mm	0.35	0.36	0.36	0.37	0.36	0.37	0.38
5 mm	0.35	0.37	0.37	0.38	0.36	0.37	0.38
15 mm	0.36	0.36	0.37	0.38	0.36	0.38	0.38

Table 2.6 Injury risk (IR) values for OI type I pediatric bone. Risk increases as value approaches 1. GMed = gluteus medius; GMax = gluteus maximus. Increases in muscle activation levels are from the baseline “normal” level.

Bowing	Muscle Activation Level						
	Normal	GMed +10%	GMed +15%	GMed +20%	GMax +10%	GMax +15%	GMax +20%
0 mm	0.66	0.67	0.68	0.69	0.68	0.69	0.70
5 mm	0.66	0.69	0.70	0.71	0.68	0.69	0.70
15 mm	0.67	0.69	0.70	0.71	0.69	0.70	0.71

Table 2.7 Injury risk (IR) values for OI type III pediatric bone. Risk increases as value approaches 1. GMed = gluteus medius; GMax = gluteus maximus. Increases in muscle activation levels are from the baseline “normal” level.

Bowing	Muscle Activation Level						
	Normal	GMed +10%	GMed +15%	GMed +20%	GMax +10%	GMax +15%	GMax +20%
0 mm	0.79	0.81	0.81	0.82	0.81	0.82	0.84
5 mm	0.79	0.82	0.83	0.84	0.81	0.82	0.83
15 mm	0.80	0.82	0.84	0.85	0.82	0.83	0.84

In the normal bone and OI type I bone, a 15 mm lateral bowing with baseline muscle forces had the same percent increase in the IR value as the femurs with no bowing and a 10% increase in the gluteus medius muscle forces. This effect was also seen in the normal bone when comparing the model of maximum lateral bowing with baseline muscle forces to the no bowing with a 10% increase in the gluteus maximus force. The type of bone modeled affected the trends in the models' response to increased parameter changes, but the increases in muscle forces had a greater overall impact on IR than increasing bowing (Tables 2.8-2.10).

Table 2.8 Percent increases of IR for normal pediatric bone. The bowing level of 0 mm with normal muscle activation levels was used as the original value in the calculations. GMed = gluteus medius; GMax = gluteus maximus. Increases in muscle activation levels are from the baseline “normal” level.

Bowing	Muscle Activation Level						
	Normal	GMed +10%	GMed +15%	GMed +20%	GMax +10%	GMax +15%	GMax +20%
0 mm		2.86	2.86	5.71	2.86	5.71	8.57
5 mm	0.00	5.71	5.71	8.57	2.86	5.71	5.71
15 mm	2.86	2.86	5.71	8.57	5.71	8.57	8.57

Table 2.9 Percent increases of IR for OI type I pediatric bone. The bowing level of 0 mm with normal muscle activation levels was used as the original value in the calculations. GMed = gluteus medius; GMax = gluteus maximus. Increases in muscle activation levels are from the baseline “normal” level.

Bowing	Muscle Activation Level						
	Normal	GMed +10%	GMed +15%	GMed +20%	GMax +10%	GMax +15%	GMax +20%
0 mm		1.52	3.03	4.55	3.03	4.55	6.06
5 mm	0.00	4.55	6.06	7.58	3.03	4.55	6.06
15 mm	1.52	4.55	6.06	7.58	4.55	6.06	7.58

Table 2.10 Percent increases for OI type III pediatric bone. The bowing level of 0 mm with normal muscle activation levels was used as the original value in the calculations. GMed = gluteus medius; GMax = gluteus maximus. Increases in muscle activation levels are from the baseline “normal” level.

Bowing	Muscle Activation Level						
	Normal	GMed +10%	GMed +15%	GMed +20%	GMax +10%	GMax +15%	GMax +20%
0 mm		2.53	2.53	3.80	2.53	3.80	6.33
5 mm	0.00	3.80	5.06	6.33	2.53	3.80	5.06
15 mm	1.27	3.80	6.33	7.59	3.80	5.06	6.33

Contour plots of the maximum principal stress distribution on the FE models of the femurs show the location of the highest stress levels. The maximum principal stress locations correspond to the area of the femur at greatest risk of injury. All of the femur models exhibit the same maximum principal stress location being the lateral femoral diaphysis, distal to the midpoint or lateral curve apex in the cases with lateral bowing (Figure 2.4).

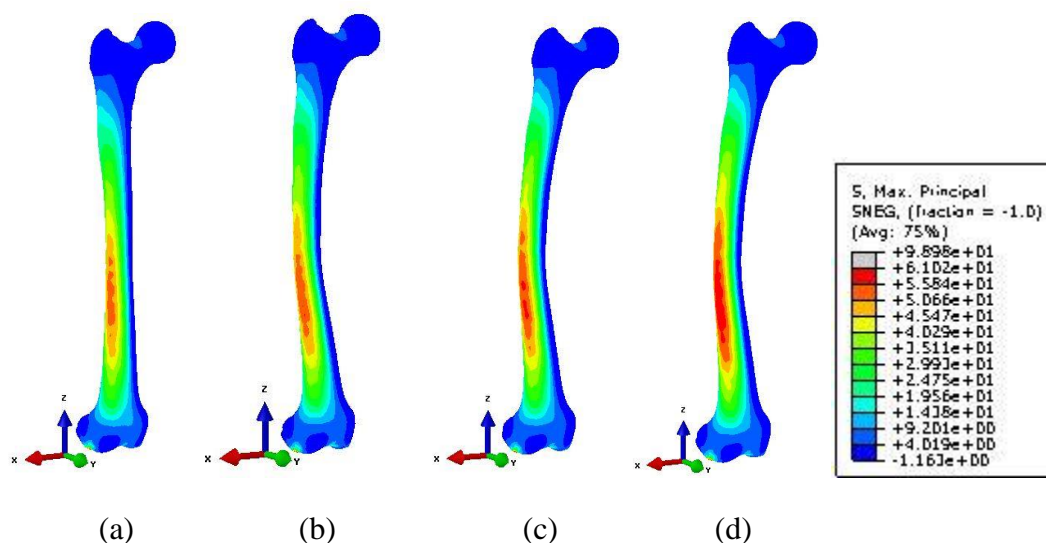


Figure 2.4 Contour plots of maximum principal stress distribution and levels (red = high, blue = low). A sample of various model results: (a) normal bone and muscle forces with no bowing, (b) normal bone and muscle forces with 15 mm lateral bowing, (c) OI type III bone with normal muscle forces and 15 mm lateral bowing, and (d) OI type III with gluteus medius force increased 20% above normal and 15 mm lateral bowing. All models are scaled to the same maximum principal stress legend (right) in units of MPa.

Statistical analyses using Welch's t-test showed significant differences in maximum principal stress values between OI type I and normal bone as well as OI type III and normal bone (Table 2.11). There were significant differences in IR values between all bone types (Table 2.12).

Table 2.11 Results of statistical analysis of maximum principals stress values between bone types. Maximum stress values are reported in MPa as mean (+ one standard deviation). A * denotes a significant difference at an alpha level of 0.05.

Bone Type	Maximum Principal Stress (MPa)	p-values		
		OI I vs OI III	OI I vs Normal	OI III vs Normal
<i>Normal</i>	57.75 (1.38)	0.212	*0.044	*0.005
<i>OI Type I</i>	58.62 (1.27)			
<i>OI Type III</i>	59.07 (1.13)			

Table 2.12 Results of statistical analysis of injury risk (IR) values between bone types. Maximum stress values are reported as mean (+ one standard deviation). A * denotes a significant difference at an alpha level of 0.05.

Bone Type	IR	p-values		
		OI I vs OI III	OI I vs Normal	OI III vs Normal
<i>Normal</i>	0.37 (0.01)	*0.000	*0.000	*0.000
<i>OI Type I</i>	0.69 (0.02)			
<i>OI Type III</i>	0.82 (0.02)			

2.4. Discussion

This study aimed to examine the impacts of geometry alterations and musculoskeletal loading on the fracture risk level of the femur. While the impacts of both parameters have been examined previously, they have not yet been examined on the current FE model and their effects on bone stress have not been compared [66, 73]. Like the current study, the boundary conditions for the prior studies represent the midstance phase of the gait cycle. However, both muscle force and bowing parameters were

analyzed on FE models that contained femoral properties based on nanoindentation data. Those models were only a representation of OI type I and had a cortical bone Young's modulus of 17 GPa compared to the current model's longitudinal modulus of 7.4 GPa. Prior models were also developed as an isotropic material [14, 22-24, 71, 73]. My original model from 2009 showed that the sensitivity of femoral stresses to gluteus medius and gluteus maximus muscle forces were meshed with tetrahedral elements rather than the current method of using hexahedral elements. This study showed that changes in forces from gluteus medius and gluteus maximums activation affect the femoral stresses during the midstance phase of gait [66]. My previous work examining the effects of increased lateral bowing on OI femur stress employed a hexahedral mesh like the current study, but used the material properties from nanoindentation like the original model. This study showed a linear increase in stress as lateral bowing increased [73]. Both of these prior studies assessing muscle forces and lateral bowing used a difference fracture criteria than the current study. Prior studies examined von Mises stress since the knowledge at the time indicated that OI bone was, in fact, an isotropic material [14, 71, 73]. These model differences do not allow for direct comparisons to be made. As the femoral FE model evolved to represent the current knowledge of OI bone exhibiting transversely isotropic properties, we performed a study to examine the effect of this change on the model output. They showed that only varying the material type to be transversely isotropic versus isotropic led to a maximum principal stress ten percent higher in the transversely isotropic femur [74].

Orthopaedic management of long bone deformities in OI includes surgical correction of deformities as a fracture prevention measure [15, 21]. The three levels of

bowing that were modeled for this study represent normal femoral geometry or what a deformity correction would achieve with a lateral bowing level of 0 mm, mild lateral bowing that would not typically illicit surgical correction of 5 mm and a level of bowing that would generally be surgically corrected of 15 mm. The increases in muscle activation represent incremental increases in force levels that would reasonably be expected with increased walking speed, running or activities such as stair ascension that would require more gluteus muscle activation than normal ambulation [87, 88]. The iterations in bowing are clinically representative of mild and severe cases while the increases in muscle forces represent functional activities.

As expected, increasing the force from the gluteal muscle activation had a greater impact on the maximum principal stresses and fracture risk levels than did increases in lateral bowing. As shown in Tables 2.3-2.6, normal bone showed a greater percent increase in maximum principal stress than OI type I and OI type III. OI type III showed the lowest percent increase in maximum principal stress of the bone type models. However, the stress levels in OI bone were much closer to their respective yield strengths than was normal bone. While the stress levels between the three bone types were not widely varied, those levels put OI bones at much higher risk of permanent injury due to their compromised mechanical properties. OI type III bone reached a maximum IR value of 0.85, OI type I bone had a maximum IR of 0.71 and the highest IR value of normal bone was only 0.38. These differences were found to be statistically significant at a level of $p=0.05$. This coincides with the vast differences seen in the respective yield strengths of OI type III, OI type I and normal bone being 72 MPa, 85 MPa and 157 MPa. The yield data came directly from mechanical testing of age- and gender-matched bone specimens

and represents the most accurate material data available. These FEA models not only present the impact of muscle forces on bone injury and, ultimately, fracture risk, but also underscore the need to fully understand the mechanical properties of OI bone.

Anecdotally, OI type III and OI type I femurs with a lateral bowing of 25 mm were modeled to see how their resultant stresses compared to those of the models with increased muscle forces. Clinically, a femur with that much bowing would generally be surgically corrected due to its qualitative risk of fracture. In both OI types, the maximum principal stress of a femur with 25 mm of lateral bowing was less than that of a femur with no bowing but a gluteus maximus force increase 10% above the level of normal ambulation. This stress was found to be between the 10% and 15% increase of the gluteus medius force of the OI femurs without lateral bowing. While these force increases are unlikely to be seen in normal ambulation, they could be achieved during running or strengthening exercises. A study of gluteus medius and gluteus maximus strengthening exercises in healthy young adults showed the forces produced by each muscle during various activities. MacAskill et al. reported the gluteus medius produces a force during side lying non-bodyweight, resisted abduction exercises that was approximately 40% higher than both forward and lateral step ups [88]. The force from resisted side lying abduction would be even higher compared to those produced during normal ambulation. MacAskill et al. also reported that prone resisted hip extension with the knee flexed to 90° produced a gluteus maximus force 70-75% higher than front and side step ups [88]. Based on these results, prone hip extension and side lying hip abduction exercises are potentially dangerous activities for a person with OI as they would load the femur closer to bone injury levels or beyond. However, these activities would not have joint loading

from ground reaction forces. It is difficult to know the exact impact of isolated strengthening and any additional role antagonist muscles and resistance may play without modeling these conditions.

Ellis et al. reported on the propulsive and braking contributions of lower body muscles during walking and running. They concluded that the gluteus maximum is one of the major propulsion muscles during walking and running while the gluteus medius is a supplemental propulsive force during high stress situations. This study also showed increased gluteus maximus recruitment during running compared to walking [87].

These findings could be impactful in rehabilitation and strengthening protocols as well as activity modifications or restrictions. Other criteria that could be considered in future modeling analyses include energy and fatigue. While the loading on the femur during a single step may not be enough to cause bone to exceed its yield strength, it is unknown how repetitive loading affects OI bone during ambulation or any activity. Future work should also incorporate results from OpenSim models to have a better idea of the forces produced by muscles during gait in persons with OI. To date, OpenSim modeling has not been used to help supply input data for FE fracture prediction models. It is now starting to be applied by our group from gait data of children and adolescents with OI, which has not yet been done. Additional analyses should also look at varying cortical thickness of the femoral diaphysis. Persons with OI have been shown to have abnormally thin cortical layers along the diaphysis of long bones [4, 16, 81]. Assessing the impact of cortical thickness on injury risk to the femur will provide much-needed insight into the necessity of using patient-specific 3D models reconstructed from MRI or CT scans or measuring cortical thickness on planar x-rays and assuming circumferential uniformity.

Cortical thickness is an important parameter as this has been shown to be affected by bisphosphonate treatments, which are often a standard care in children with OI. Assessing femur injury risk should additionally include FEA of activities that children typically do which may cause fracture, such as running, jumping, kicking and falling. These higher force activities are most applicable in mild to moderate forms of OI rather than severe OI.

3. Muscle Firing Pattern Variations between a Population with OI Type I and an Age- and Gender-Matched Control Population

3.1. Background

The goal of this study was to test the hypothesis that ambulatory children and adolescents with OI type I exhibit significantly difference EMG timing patterns of the gluteus medius and gluteus maximus than age- and gender-matched controls. This was tested by performing clinical gait analysis on a group of each population. Previous work by Graf et al. showed that children with OI type I exhibit significant differences in some gait parameters compared to their age-matched control peers [85]. The population with OI type I spent a larger portion of the gait cycle in double limb support and also had delayed foot off, thus had a longer stance phase than the control population. The extended stance phase seen in the OI population most likely contributed to the significantly delayed timing of the peaks of stance phase hip extension, stance phase knee extension, swing phase knee flexion, stance phase external foot progression angle, ankle push off moment, ankle power absorption and ankle power generation. Significantly decreased ankle plantarflexion (3rd rocker), stance phase ankle range of motion (ROM), stance phase minimum pelvic downward obliquity, ankle power absorption and ankle power generation (push off power) was also seen in the OI group [85]. While this work established differences between temporal, kinematic and kinetic gait parameters, it did not report on differences seen in muscle timing patterns from surface electromyography (EMG). Typical clinical gait analysis includes surface EMG electrodes on four muscles bilaterally: 1) tibialis anterior, 2) medial head of the gastrocnemius, 3) medial hamstrings (semitendinosus) and 4) rectus femoris. Based on the data from Graf et al. regarding the

delayed timing in gait cycle peaks and previous work by myself showing the sensitivity of femoral surface stress to changes in gluteal muscle forces, this gait study added surface EMG electrodes to the gluteus medius muscles, bilaterally [66, 85]. Analyzing the timing of muscle firing and their patterns during gait will provide further insight into ambulatory differences in persons with OI compared their control peers. This information directly contributes to the femoral fracture risk FE models in OI.

3.2. Methods

3.2.1. Data Collection

Twenty participants were recruited and signed written informed consent/assent to participate in the study protocol approved by the Rush University/Shriners Hospitals for Children, Chicago and Marquette University Institutional Review Boards. Gait analysis was performed at the Motion Analysis Laboratory (MAL). The MAL (Figure 3.1) includes a 14-camera



Figure 3.1 The Motion Analysis Laboratory at Shriners Hospitals for Children – Chicago. Two of the fourteen Vicon cameras are circled and labeled. The four AMTI force plates are outlined and labeled along the lab’s walkway. The positive x-direction is labeled at the bottom of the photo.

Vicon MX motion analysis system (Vicon Motion Systems, Ltd; Oxford, UK), four six-axis AMTI OR6-5-1 force plates (Advanced Mechanical Technology, Inc.; Watertown,

MA) embedded in the middle of a 30 foot long walkway and a 16-channel Delsys Trigno (Delsys, Inc.; Natick, MA) wireless EMG system.

The study population was comprised of ten children and adolescents with OI type I (six females, four males; 9 ± 4.99 years) and ten age- and gender-matched peers (six females, four males; 10 ± 4.50 years). Subjects were instrumented with 17 reflective markers and ten surface EMG electrodes affixed to their skin with hypoallergenic tape for dynamic data collection (Figure 3.2). The EMG data was collected bilaterally from the gluteus

maximus, gluteus medius, rectus femoris, medial hamstring, tibialis anterior, and medial gastrocnemius muscles. A Newington-Helen Hayes marker set (Table 3.1) was used for this study in accordance with Vicon's Plug-in Gait model [90]. This marker set utilizes a knee alignment device (KAD) and a medial malleolus marker, bilaterally, for calculation of tibial rotation. Without the medial malleoli markers, using the KAD leads to the system assuming the ankle flexion axis parallels the knee flexion axis [90].



Figure 3.2 Instrumented motion analysis subjects. Top: Anterior (left), posterior (middle) and lower leg (right) views of a 6-year-old male control subject. Bottom: Anterior (left), posterior (middle) and lower leg (right) views of a 6-year-old male OI type I subject.

Each subject had an initial static trial collected prior to dynamic data acquisition. The static trial was acquired as the subject stood on one of the force plates while facing the positive x-direction of the lab's coordinate system (Figure 3.1). Following the static trial, the medial malleoli markers and KADs were removed and knee markers were placed on the lateral femoral epicondyles bilaterally. Dynamic trials were collected while the participants walked at a self-selected speed along the walkway. Data collection from the cameras, EMG electrodes and force plates were synchronized through Vicon's Nexus software. A minimum of six trials with at least one clean force plate strike were collected, with no more than 20 trials being collected per subject.

Table 3.1 Marker set used for gait analysis.

Marker Name	Marker Location
LASI	Left anterior superior iliac spine (ASIS)
RASI	Right anterior superior iliac spine (ASIS)
SACR	Sacrum; junction of the L5/sacral vertebrae midway between the posterior superior iliac spines (PSIS)
LTHI	Left thigh; placed on the left patella, labeled as "LTHI" for the model
LKAX*	Left KAD marker that points laterally
LKD1*	Left top KAD marker
LKD2*	Left bottom KAD marker
LKNE ⁺	Left knee; lateral femoral epicondyle
LTIB	Left tibia; upper 1/3 of the tibia on the lateral side, in line with the knee and ankle flexion axes
LANK	Left ankle; lateral malleolus apex
LHEE	Left heel; calcaneal tuberosity
LTOE	Left toe; head of the 2 nd metatarsal at the same height as the heel marker
LMED	Left medial malleolus apex
RTHI	Right thigh; placed on the right patella, labeled as "RTHI" for the model
RKAX*	Right KAD marker that points laterally
RKD1*	Right top KAD marker
RKD2*	Right bottom KAD marker
RKNE ⁺	Right knee; lateral femoral epicondyle
RTIB	Right tibia; upper 1/3 of the tibia on the lateral side, in line with the knee and ankle flexion axes
RANK	Right ankle; lateral malleolus apex
RHEE	Right heel; calcaneal tuberosity
RTOE	Right toe; head of the 2 nd metatarsal at the same height as the heel marker
RMED	Right medial malleolus apex

*Indicates marker used only for static trial

⁺Indicates marker used only for dynamic trial (replaces KAD)

3.2.2. Analysis

All gait trials were processed with Vicon's Plug-in-Gait model using Nexus 1.8.5 software. Gait cycle events (foot strike and foot off) were labeled. Due to data collection issues, some of the subjects' data could not be included. In the control population, a total of fourteen legs were assessed for both the gluteus medius and gluteus maximus muscles. There were nineteen legs for the gluteus medius and twenty legs for the gluteus maximus in the OI population. The EMG data was processed using a linear envelope with a 6 Hz cutoff frequency for each trial. Each subject's trials were checked for consistency and any outliers were removed. The average linear envelope data of the right and left gluteus medius and gluteus maximus for each subject was plotted (Figures 3.3 and 3.4). This plot was used to calculate the threshold (y_t) for determining muscle on/off activation using Eqn 3.1 based on work by Di Fabio et al:

$$y_t = \mu + \sigma J \quad (3.1)$$

In this equation, μ is the mean, σ is the standard deviation and J is a constant set to 3 for this data [91]. This equation was applied to the data when the muscle was at rest. Each muscle was determined to be "on" when its linear envelope value was equal to or exceeded y_t and "off" when this value was below y_t . A single subject's plot of one muscle in Figure 3.5 shows the detail of the graphs used to determine the activation timing. The on/off points were recorded as a percentage of gait cycle for both legs for each subject. One-tailed Welch's t-tests with an alpha level of 0.05 were performed on the data to determine if there were significant differences. This was first done within each population between the left and right sides to look for asymmetry between sides. If no asymmetry was present, the population data was grouped together to compare the control

versus OI data. The same approach was applied to the temporal spatial gait parameters of cadence, foot off timing, double limb support, stride length and walking speed. The activation timing of the muscles was also compared to published normal data. Temporal-stride parameters were also analyzed between the two groups.

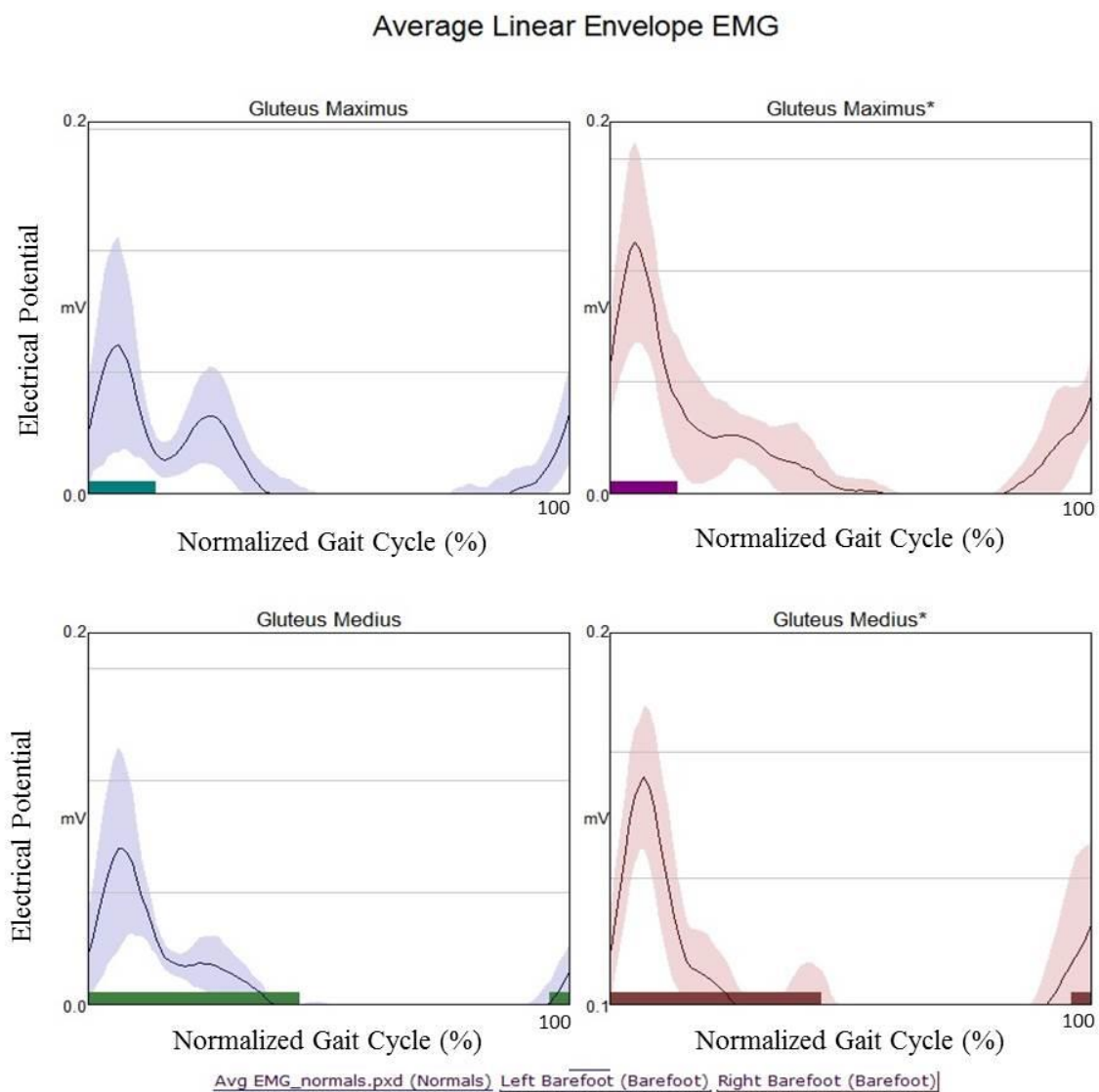


Figure 3.3 Representative control population EMG data. Average (with shaded standard deviation) linear envelope EMG plots from a 6-year-old male control subject. Left is represented in blue, right is represented in red. Solid bars along the x-axis indicate when the muscle is expected to be active. The y-axis is electrical potential (mV). The x-axis is normalized gait (%) from 0-100.

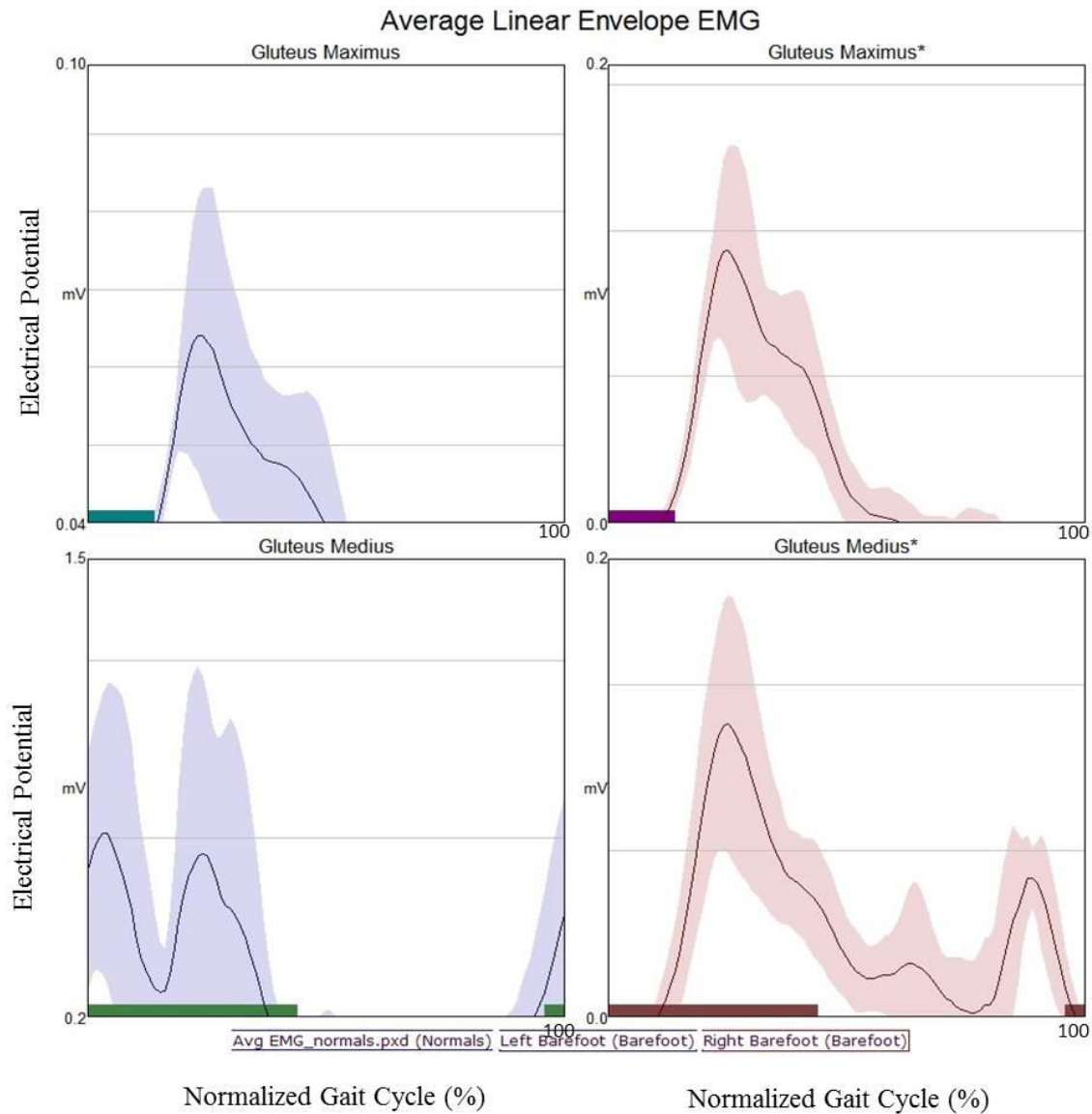


Figure 3.4 Representative OI population EMG data. Average (with shaded standard deviation) linear envelope EMG plots from a 6-year-old male with OI type I. Left is represented in blue, right is represented in red. Solid bars along the x-axis indicate when the muscle is expected to be active. The y-axis is electrical potential (mV). The x-axis is normalized gait (%).

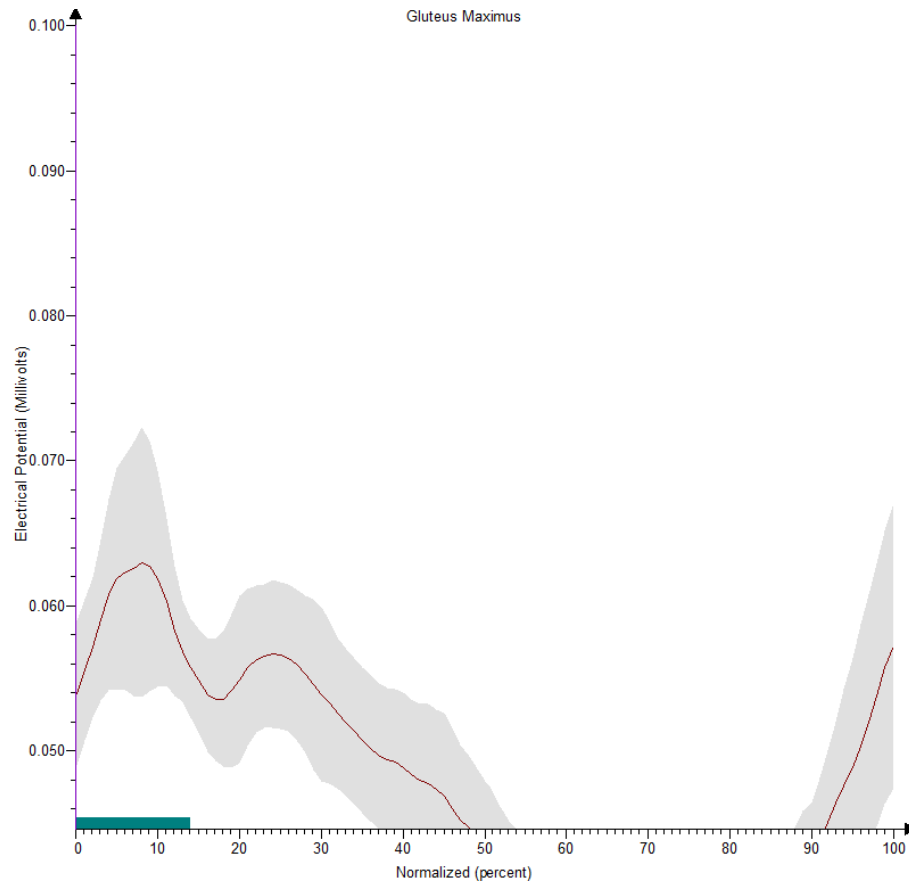


Figure 3.5 The right glutueus maximus plot of one subject. The y-axis minimum was set to the y_t value for this muscle (0.045).

3.3. Results

Temporal-stride parameters were assessed and compared between groups for significant differences. The OI population showed significantly longer double limb support time and slower walking speed at an alpha level of 0.05 compared to the control population (Table 3.2).

Table 3.2 Temporal spatial gait parameters comparison between control and osteogenesis imperfecta type I (OI) populations. A * indicates a significant p-value with an alpha level of 0.05. Gait cycle = GC.

		Mean	Standard Deviation	P-Value
Cadence (steps/min)	<i>Control</i>	136.14	15.27	0.1588
	<i>OI</i>	131.45	9.21	
Foot Off (%GC)	<i>Control</i>	59.11	1.25	0.0883
	<i>OI</i>	59.94	2.19	
Double Limb Support (%GC)	<i>Control</i>	18.01	1.96	*0.0026
	<i>OI</i>	20.08	1.96	
Stride Length (m)	<i>Control</i>	0.98	0.20	0.1055
	<i>OI</i>	0.90	0.16	
Walking Speed (m/s)	<i>Control</i>	1.10	0.15	*0.0167
	<i>OI</i>	0.98	0.16	

Muscle on/off timing and duration were examined between the control and OI subjects for differences. Statistical analysis within each population showed no significant differences at an alpha level of 0.05 between the left and right sides for the gluteus medius and gluteus maximus muscles during gait (Tables 3.3 and 3.4). Therefore, the sides were grouped for comparison between the control and OI population data. This data showed only one significant difference; initial activation of the gluteus maximus was delayed in the OI group compared to the age- and gender-matched controls (Table 3.5).

Table 3.3 Gluteus medius EMG timing comparison between sides. Timing is expressed as a percentage of the gait cycle (GC).

Control		Mean (% GC)	Standard Deviation	P-Value
On	<i>Left</i>	0.5	1.4	0.1780
	<i>Right</i>	0.0	0.0	
Off	<i>Left</i>	45.0	9.6	0.2094
	<i>Right</i>	38.9	16.4	
On	<i>Left</i>	80.7	18.9	0.1679
	<i>Right</i>	88.4	4.4	
On Duration	<i>Left</i>	44.4	10.3	0.2341
	<i>Right</i>	38.9	16.3	
Off Duration	<i>Left</i>	35.7	23.1	0.2480
	<i>Right</i>	43.3	13.9	
OI Type I		Mean (%GC)	Standard Deviation	P-Value
On	<i>Left</i>	0.7	2.3	0.3773
	<i>Right</i>	1.2	3.5	
Off	<i>Left</i>	38.3	13.0	0.1138
	<i>Right</i>	48.6	20.9	
On	<i>Left</i>	91.0	15.4	0.1533
	<i>Right</i>	78.8	26.5	
On Duration	<i>Left</i>	37.5	14.2	0.1325
	<i>Right</i>	46.4	18.3	
Off Duration	<i>Left</i>	52.3	22.2	0.1116
	<i>Right</i>	34.3	24.9	

Table 3.4 Gluteus maximus EMG timing comparison between sides. Timing is expressed as a percentage of the gait cycle (GC).

Control		Mean (% GC)	Standard Deviation	P-Value
On	<i>Left</i>	0.2	0.5	0.1780
	<i>Right</i>	0.0	0.0	
Off	<i>Left</i>	34.9	12.1	0.4640
	<i>Right</i>	35.6	15.0	
On Duration	<i>Left</i>	34.7	11.9	0.4538
	<i>Right</i>	35.6	15.0	
OI Type I		Mean (% GC)	Standard Deviation	P-Value
On	<i>Left</i>	1.8	4.4	0.1784
	<i>Right</i>	6.0	12.9	
Off	<i>Left</i>	36.6	11.4	0.3296
	<i>Right</i>	33.2	20.7	
On Duration	<i>Left</i>	34.7	10.9	0.0881
	<i>Right</i>	27.2	12.9	

Table 3.5 Gluteus medius and gluteus maximus EMG timing comparison between control and osteogenesis imperfecta type I (OI) populations. Timing is expressed as a percentage of the gait cycle (GC). A * indicates a significant p-value.

<u>Gluteus Medius</u>		Mean (% GC)	Standard Deviation	P-Value
On	<i>Control</i>	0.3	1.0	0.1803
	<i>OI</i>	0.9	2.8	
Off	<i>Control</i>	42.0	13.2	0.4123
	<i>OI</i>	43.2	17.5	
On	<i>Control</i>	83.9	14.8	0.4201
	<i>OI</i>	85.3	21.4	
On Duration	<i>Control</i>	41.7	13.4	0.4996
	<i>OI</i>	41.7	16.5	
Off Duration	<i>Control</i>	38.9	19.4	0.2321
	<i>OI</i>	45.3	24.0	
<u>Gluteus Maximus</u>		Mean (% GC)	Standard Deviation	P-Value
On	<i>Control</i>	0.1	0.4	*0.0461
	<i>OI</i>	3.9	9.6	
Off	<i>Control</i>	35.2	13.1	0.4718
	<i>OI</i>	34.9	16.4	
On Duration	<i>Control</i>	35.1	13.0	0.1770
	<i>OI</i>	31.0	12.2	

The stance phase activation and termination of the gluteus medius in both groups was very similar to normal on/off timing of 0% and 40%, respectively. However, the swing phase activation occurs early in both groups at approximately 85% compared to the normal timing of 96%. Normal on/off timing of the gluteus maximus is 0% and 14%, respectively. The OI type I group had delayed activation. Both groups had an average end of activation around 35%.

3.4. Discussion

Previous gait analysis on children with OI type I showed that they exhibit a delayed foot off and increased time in double limb support speed than their age-matched

control peers [85]. Therefore, it was expected that muscle activation timing of the gluteus medius and gluteus maximus muscles would be significantly different between adolescents with OI type I and a control population of their age- and gender-matched peers with prolonged activation duration. This study did not show a significant difference in foot off timing, though the data trended to a delay in the OI population. In agreement with previous assessments, the OI group of this study showed a longer time in double limb support than the control population. Longer time in double limb support is a strategy employed to provide a more stable base. This is also associated with slower walking speeds and may be a compensatory or, at least, cautionary mechanism of ambulation in children with OI. Unlike the previous study, the data from this study showed a significantly slower walking speed in the OI group compared to the healthy control group. This was a qualitative trend in the study by Graf et al, but not a significant difference at an alpha level of 0.05 [85]. Changes in walking speed often alter muscle activation. A study by Shin et al. examined the changes in gluteus maximus force with changes in walking speed in healthy young adults. They reported a 7% increase in gluteus maximus force between walking speeds of 1.5 km/h and 3.5 km/h. The study also showed a nearly 10% increase in gluteus maximus force between walking speeds of 3.5 km/h and 5.5 km/h. This resulted in an 18% increase of the gluteus maximus force between the slowest and fastest walking speeds [89]. The average walking speed of the OI group was approximately 3.5 km/h, which is the same as the middle speed tested by Shin et al. This increased activation force of the gluteus medius has been tied to the increase in arm swing seen with increased walking speeds [89, 92].

Preliminary results of a characterization of gait kinematics in children with OI types I, IV and III indicate a pattern of excessive hip abduction during stance. This pattern could indicate increased gluteus medius activation force during stance since it is the primary hip abductor. However, the only significant difference in the EMG data of the gluteus muscles during ambulation was delayed gluteus maximus activation in the OI population compared to controls. A prior examination of muscle timing in a single adolescent with OI type I showed prolonged hamstring activity during stance compared to reported normal values. At the time, it was theorized that this may partially be a mechanism to avoid or reduce gluteus muscle firing and partially due to a slower walking speed than typically developing peers [14, 66, 93]. While the timing of the hamstrings was not analyzed in this study, the finding of delayed gluteus maximus activation may warrant examination of the hamstrings to see if they exhibit prolonged activity. Prolonged hamstring activity combined with delayed gluteus maximus activity may indicate an internal protective mechanism to reduce femur loading during ambulation. The study of muscle characteristics and strength is relatively new to the OI field. It has been theorized that the inherent bone fragility in OI may be, in part, associated with deficits in muscle function [94]. A study of children with OI found that while muscle cross-sectional areas were reduced compared to age- and gender-matched controls, there was no difference in density. This study calculated specific force (force per unit of muscle cross-sectional area) to account for the smaller muscle sizes in OI. It was found that, on average, the children with OI had a specific force generation that was 16% lower than that of their control population peers [94]. Another study of ankle strength reduced strength between children with OI type I and age-matched controls. Additionally, the

children with OI had significantly reduced push-off power during gait compared with their age-matched peers. This study indicates that children with OI may have benefit from strengthening programs [95]. Muscle strength is highly correlated with gait and physical function and the ability of children with OI to actively participate with their peers [96]. A pilot study performed at Shriners Hospitals for Children – Chicago showed a nearly 300% increase in plantar flexor strength was achieved after four weeks of a functional strengthening protocol in a children with OI type I. This preliminary data along with a prior study by Caudill et al. indicate that focused strength training programs may allow children with OI to perform more advanced activity skills such as running, jumping, stairs and increased walking speed and efficiency [95]. Along with these functional strengthening paradigms focused on improving plantar flexor strength to increase push-off power and, subsequently, walking speed, the accompanying increased activation forces from the gluteus medius and gluteus maximus should also be monitored to ensure the levels of bone stress are not putting them at risk for injury or fracture. This could be accomplished through the combination of gait analysis, musculoskeletal modeling with OpenSim and FE models. The combination of these methodologies could provide more insight into patient-specific muscle forces, joint loading and skeletal stress and strain distributions during ambulation.

4. Analysis of Model Geometry Development: Individual Computed Tomography (CT) Scan versus Biplanar X-ray Scaling

4.1. Background

Model geometry is an important part of patient- or subject-specific FEM. This becomes especially significant when modeling persons with bone deformities or abnormal geometries. Standard models are based on normal long bone size, shape and material distribution. All of these are altered in OI bones. Prior OI femur models have used x-rays to match geometry to a standard model [14, 71]. The current OI tibia model uses the same x-ray matching technique combined with 3D reconstructions of pQCT images of the distal tibia [75]. Most long bone fractures in OI occur in the diaphysis region [81]. This is likely due in part to the reduced cross sectional area from the thin cortices that are characteristic of long bones in OI.

4.2. Methods

4.2.1. Model Development

This study created and analyzed two FE models of the diaphysis region of the right femur of a 10-year-old female with OI type III. The diaphysis region was modeled for this study because the majority of fractures occur in this region and the purpose of this study was to evaluate and initial model comparison. The models were the same length and had the same mid-diaphyseal width. They were both defined with the same solid, elastic material properties defined by engineering constants (Table 4.1).

Table 4.1 Material property assignments for femoral diaphysis models. E is Young's modulus, ν is Poisson's ratio, and G is shear modulus.

	Transverse			Longitudinal		
	E (GPa)	ν	G (GPa)	E (GPa)	ν	G (GPa)
Cortical	3.7	0.3	1.4	5.7	0.3	2.2
Cancellous	1.1	0.2	0.5	1.7	0.2	0.7

The femoral diaphysis models were both fixed in all directions, translations and rotations, at the distal end to prevent free-body rotation. An axial load of 156 N was applied to a centrally located node on the the proximal end of each model. The models differed in their geometry origination and appearance. The first model was developed from a clinical CT scan of the patient's lower body when she was 10 years, 2 months of age, 90.45 cm tall and weighed 15.75 kg. The second model was developed by scaling a 3D reconstruction of a healthy adult femur to match the length and mid-diaphyseal width of the patient's femur. The CT scans has been previously clinically acquired with a slice thickness of 1.5 mm. The resulting images had a pixel size of 0.74 mm, which is an approximate resolution of 34 pixels per inch. Prior to the acquisition of the CT image, an intramedullary rod had been placed in the right femur (Figure 4.1).



Figure 4.1 A coronal plane slice of the CT of the right femur. Note artifact in mid-diaphysis from intramedullary rod.

The CT data was edited, segmented and reconstructed to create a 3D volume using Seg3D 2.2.1, which is an open source software available from the University of Utah Center for Integrative Biomedical Computing [97]. The data was imported as a volume. The coronal plane view was primarily used for segmenting the femur. Median filters and Otsu thresholds were applied to help segment the bone, metal rod and soft tissue materials. Thresholds were set manually and the painting feature was used to isolate regions. Extraction of connected components was used to remove artifact and the adjacent bones of the tibia distally and the pelvis proximally (Figure 4.2).

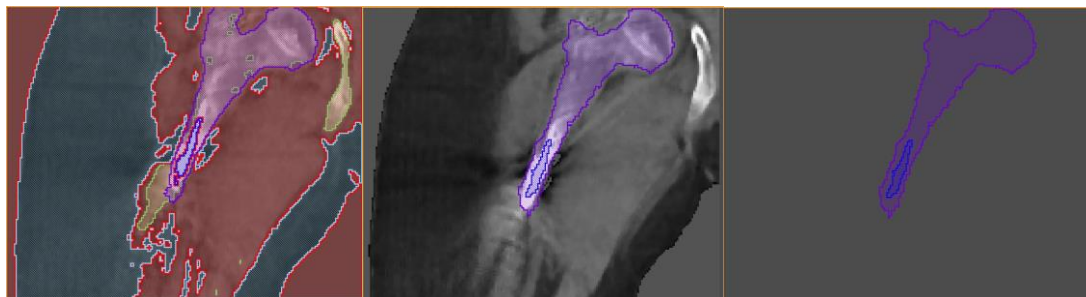


Figure 4.2 Three stages of femur segmentation in Seg3D from CT scan of a pediatric patient with OI type III. Left: Image showing segmenting of femur from soft tissue, metal rod and adjacent pelvic bone. Middle: Femur and metal rod outlined in a single coronal plane slice. Right: Femur and rod segmented from the rest of the CT image.

The Boolean operator was used to remove the rod from the femur. Due to the metal artifact and thin cortex, the volume of the segmented femur was very rough and contained holes (Figure 4.3). Smoothing and hole-filling were used to improve the solid model, but still contained “lumpy” geometry compared to a reconstructed normal femur (Figure 4.4).

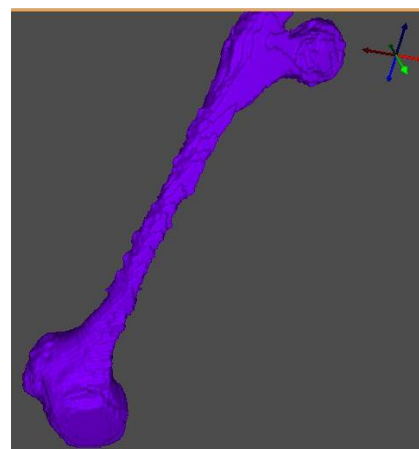


Figure 4.3 Volumetric rendering of OI femur from CT scan in Seg3D.

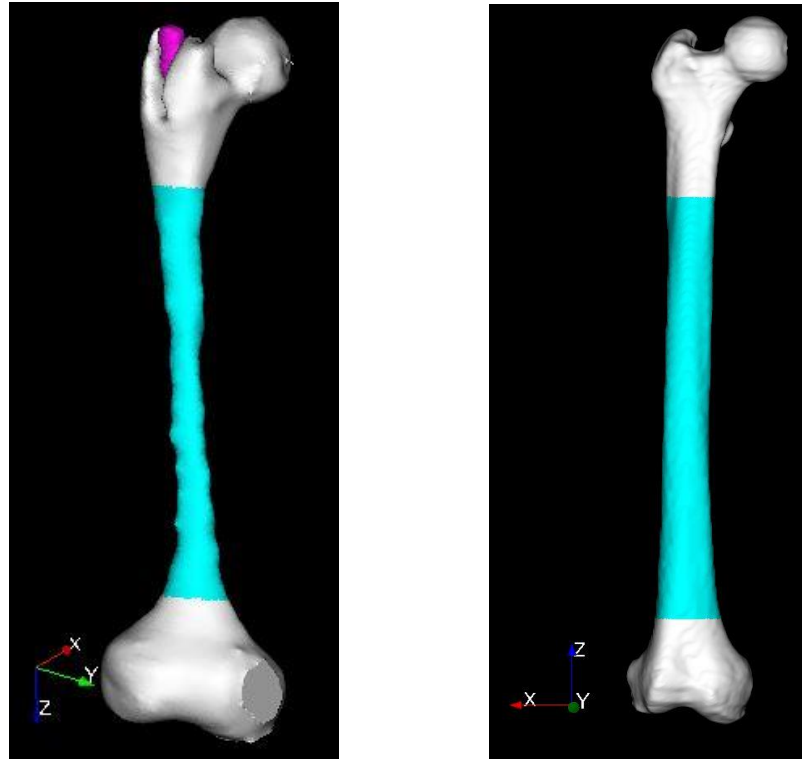


Figure 4.4 3D solid models of a pediatric femur with OI type III (left) and a normal adult femur (right). Both femur models depict the diaphysis in aqua shading. The OI femur also shows the metal rod (pink) that was extracted from the model for analysis.

Since the diaphysis was the region of interest for this study due to it being the location of fracture risk, the solid model was cut proximal to the femoral condyles and distal to the lesser trochanter so that only the femoral diaphysis assessed (Figure 4.5). IA-FEMesh was used to create the mesh based on element size seeding from a building block structure (Figure 4.6). This mesh was comprised of 2268 C3D8 type



Figure 4.5 Solid model of the diaphysis of the CT femur. Z-direction is distal, y-direction is medial and x-direction is posterior.

(hexahedral) elements, which was checked for element shape integrity through the Jacobian index in IA-FEMesh (Figure 4.7). The mesh was then exported as a “.inp” file, which is an input file for ABAQUS. A local

axis, or datum, was created within ABAQUS in order to load the diaphysis axially. This coordinate system was set up by having z be positive in the distal direction with the z-axis normal to the distal face of the diaphysis (Figure 4.8).

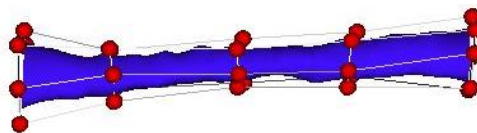


Figure 4.6 Building block structure for the CT femur model in IA-FEMesh.

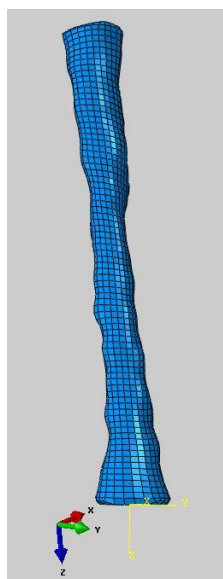


Figure 4.7 Mesh of the CT femur diaphysis.

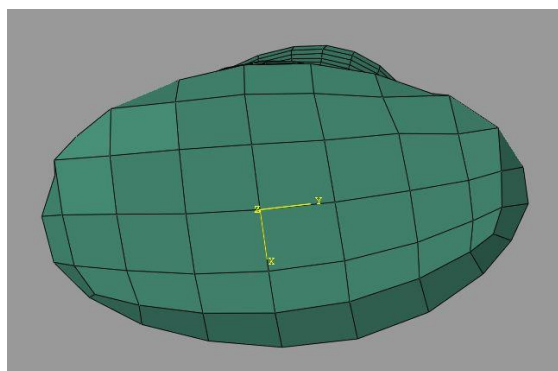


Figure 4.8 Local coordinate system for the CT femur model.

The second model originated from the same solid femur used in the first study. This solid model is of a normal, adult femur developed from a CT scan. Like the first model, this solid was also cut below the lesser trochanter and above the femoral condyles to only model the femoral diaphysis (Figure 4.9). The same meshing techniques as the first model were used, but the building block structure looked different and a coarser mesh was able to be used (Figures 4.10 and 4.11). Like the CT model, the element shape

integrity was verified by assessing the Jacobian value. This model is composed of 875 hexahedral, type C3D8 elements. For the scaled model, the global z axis was already aligned along the length of the bone with positive pointing proximally.



Figure 4.9 Solid model of the scaled femur diaphysis. Z-direction is proximal, y-direction is anterior and x-direction is lateral.

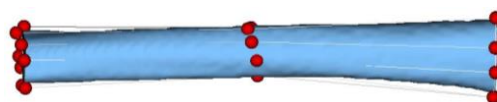


Figure 4.10 Building block structure for the scaled femur model in IA-FEMesh.

The two model meshes were both checked for convergence. Both models were assigned two sections: one to represent cortical bone and one to represent cancellous bone. The cortical bone was defined as the set of elements on the exterior of the model. The cancellous bone was defined as a set of the interior elements. Each section was assigned the same corresponding elastic material properties from engineering constants (Table 4.1) and those materials were assigned orientations based on the datum axis for the CT model and the global axis for the scaled model (1, 2, 3 \rightarrow x, y, z). Loading and boundary conditions were assigned as previously described.

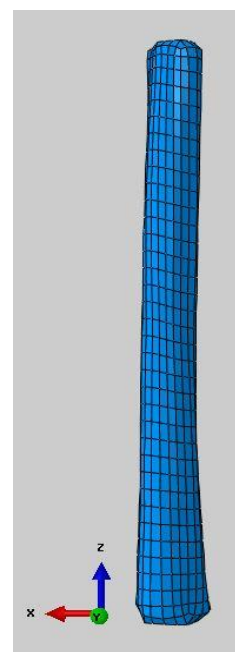


Figure 4.11 Mesh of scaled femoral diaphysis.

4.2.2. Analysis

The two FE femoral diaphysis models had stress and strain results requested as the field output request in ABAQUS. Both models were run as a quasi-static test with one step of applied loading. The quantitative and qualitative results of the scaled model were compared to the results of the model for the CT scan to examine the accuracy of the scaling method in development of FE models for bone injury risk in OI.

4.3. Results

The model from the CT scan of the femur had a peak maximum principal stress of 22.46 MPa and a peak maximum principal strain of 6.17×10^{-3} on the medial side just distal to the mid-diaphysis (Table 4.2, Figure 4.12). The model based on a CT of a normal femur scaled to match the size of the OI femur had a peak maximum principal stress of 15.71 MPa and a peak maximum principal strain of 5.35×10^{-3} on the anterior side in the middle of the diaphysis (Table 4.2, Figure 4.12). The scaled model resulted in a peak maximum principal stress that was 30% lower than the CT model. Its maximum principal strain was 13% lower than the model from the patient's CT scan.

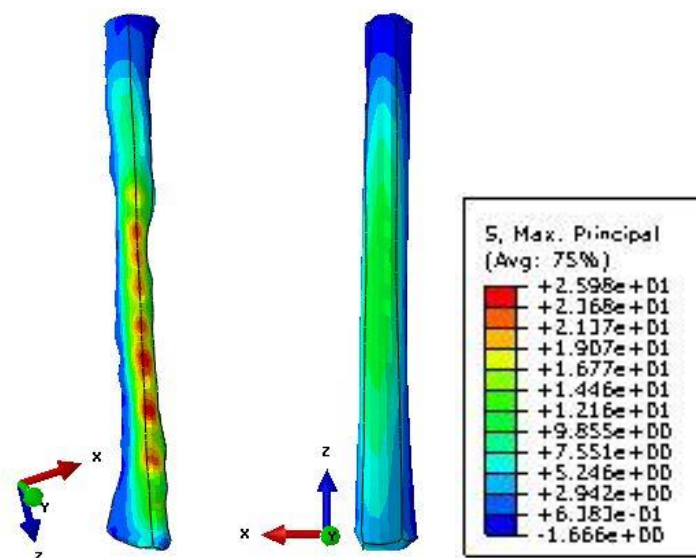


Figure 4.12 Contour plots of the maximum principal stresses for the CT (left) and scaled (right) models. The same scale was used for both models. The CT model is showing its medial side. The scaled model is showing its anterior side. Both models are shown on the same scale of maximum principal stresses in MPa.

Table 4.2 Results of femoral diaphysis models.

	Maximum Principal Stress (MPa)	Maximum Principal Strain
CT Femur Model	22.46	6.17×10^{-3}
Scaled Femur Model	15.71	5.35×10^{-3}

4.4. Discussion

This study addressed the question of how well scaling an FE model of a normal long bone diaphysis can match the geometry of an FE model created directly from a patient's 3D imaging data. While their geometries were very similar, the CT model had maximum principal stresses and maximum principal strains that were higher than those of the scaled model. The models were 117 mm long and had the same mid-diaphyseal diameter of 14 mm. Both models had a cortical thickness of approximately 3 mm. The

elements in the scaled model were about twice as large in the axial (z-direction) at 4 mm compared to 2 mm in the CT model. This difference accounts for the majority in the difference between the number of elements in the models with the CT model having 2268 elements and the scaled model having 875 elements. The scaled model had the same diameter along its entire length whereas the CT model had a wider diameter of 48 mm at its distal and proximal ends that tapered to 14 mm for most of its length. The morphology discrepancies may contribute to the differences in resulting stresses and strains of the two models. The CT model had a very rough surface even after smoothing algorithms. This was due to the minimal amount of cortical bone segmented from the femoral rod and surrounding soft tissues in the CT image. The reconstructed volume before smoothing had a stair step appearance (Figure 4.3). The segmenting was primarily performed from the coronal plane slices, but all planes were used to manually paint the edges and define the regions that were femoral bone. The CT model's bumpy surface likely contributed to the differences in the areas of highest stress and strain between the two models. Rough outer cortex surfaces have been depicted in x-rays of other OI bones [98]. The CT model exhibited its highest stresses on the medial side, just distal to the mid-diaphysis whereas the scaled model's maximum stress concentrations were located mid-diaphysis on the anterior side. The contour plots of the maximum principal stresses and strains in the scaled model make sense based on the loading application and normal femur geometry. These morphologies resulted in the elements of the FE model not being stacked directly along the axial direction in the CT model as they were in the scaled model.

The CT data used for this study was the only femoral CT available from the OI population at Shriners Hospitals for Children – Chicago who had consented to our IRB-

approved research protocols. The population size includes hundreds of children with OI. This speaks to the rarity of a child with OI receiving a clinical CT scan. It is commonly accepted that CT scans are the optimal origination for patient-specific FE models. They can provide 3D bone geometry as well as a mapping of bone material properties values and their heterogeneity throughout the bone. In this case, the CT was only used for the 3D geometry information. Obtaining bone density distribution and calculating Young's modulus from CT data typically requires the image acquisition to be calibrated with a phantom of known density. This allows the Hounsfield units from the CT scan to be converted to bone density and Young's modulus throughout the cortical and cancellous bone layers [34]. The CT scan of the OI femur was acquired clinically and was part of the patient's medical records, which was accessible to us via the IRB and signed assent and consent forms. Recently, researchers in Europe published their development of an automatic method for creating 3D models for patient-specific FEA based on single hip DXA images. Their methodology involved the creation of a statistical appearance model (SAM) as a template and reference images for shape reconstruction and matching [44]. Simply put, they used anatomical reference points and a database of morphology information to match the single DXA image to a 3D model. This is similar to the methodology employed by Caouette et al. in their FE model of the OI tibia [75]. However, these methods, like all geometry matching methods, have the potential to misrepresent complex geometry changes. The DXA scan method overestimates cortical thickness in regions of thin cortical bone, which would be an issue in OI bone [44]. Previous FE models of the femur in OI have used the techniques used to create the scaled model in this study. A standard 3D model of a femur was meshed and scaled to match the

length and lateral bowing of femur with a mild lateral bowing equivalent to 5 mm (10°). Without a patient-derived 3D image, it was unknown how well that technique represented the geometry and morphology of an OI bone. It is hard to know if that technique may be adequate for modeling patients with OI type I or IV as they do not have as severe of bone deformity as those with OI type III. Recent advances in medical imaging have made the use of magnetic resonance imaging (MRI) a potential solution to creating patient-specific 3D models in OI. MRI images do not expose patients to radiation, but would not be as feasible for patients with any metal such as fracture fixation plates or intramedullary nails. Future work could use MRI to examine the efficacy of the x-ray scaling methods in OI type I or IV without metal implants. New advances allow researchers to more easily segment bone in MRI data sets and use that data to acquire bone material properties, according to Dr. Kevin Koch at the Medical College of Wisconsin Department of Radiology. This could provide the necessary patient-specific data to make FE models of OI bones more accurate.

5. Conclusion

5.1. Study Motivation

This work aimed to provide more complete data on the effects of bowing and gluteal muscle forces on bone loading, gluteal muscle activation timing during gait and the differences in two FE models developed from different 3D geometry in children with OI. In orthopaedic management of OI, fracture risk is clinically assessed through phenotype, radiographs, bone deformity and BMD scans. This risk is based on clinical experience and current knowledge about OI bone characteristics. Phenotype gives a qualitative indication of risk as it is based on the severity level of the disorder. Children with OI type I are at a lower risk of fracture than their peers with any other OI phenotype. Radiographs, level of deformity and BMD are capable of providing quantitative information for risk assessment. Deformity is used as a measure to indicate when surgical intervention would be appropriate for fracture prevention. For example, a lateral bowing in the femur that exceeds 20° would be a candidate for surgical correction with an intramedullary nail to straighten the bone [21]. Radiographs can provide information on the degree of deformity as well as the cortical thickness in the plane of the x-ray view. Thin cortical layers have been supposed as a fracture risk in long bones of persons with OI [81]. Reduced trabecular BMD has been reported in OI with levels varying by severity and lower BMD being more indicative of weaker, more brittle bones [4, 16, 81]. Previous work was done to develop a methodology for creating patient-specific models of the femur in children with OI to provide more complete quantitative data on fracture risk [71, 76]. This model was the first to use FEA to analyze fracture risk in OI. Following the

initial model development, it was shown that the stress levels in the femur were sensitive to muscle forces from the gluteus medius and gluteus maximus and changes in lateral bowing levels [66, 73, 74, 76, 99, 100]. These works led to the development of the first two projects in this work: 1) the assessment of whether muscle forces contribute more to femoral stress levels than lateral bowing and 2) analyzing gluteus muscle activity during ambulation in children with OI and their age- and gender-matched peers.

The increased stresses in the femur with increased lateral bowing during simulation of the loading response phase of gait were not surprising since bone deformity moves more of the material away from the mechanical axis of loading. Lateral bowing, in particular, would clearly cause an increased bending moment about the femur's anterior-posterior axis of rotation. This was shown in the original and subsequent femur model's maximum stresses being tension on the lateral side of the femur around the bowing apex [71, 76]. However, the FE femur model's sensitivity to gluteus medius and gluteus maximus forces was not expected. Analysis of the results made sense of the gluteal muscle force contribution when the attachment points of both muscles and their lines of action were considered. Like lateral bowing, increasing their force levels would cause an increased bowing moment and, thus, increase the tensile stress along the lateral side of the femur in the mid-diaphysis region. While these two parameters had been looked at independently in various stages of the model development, their comparative impact had not yet been considered. There has been recent focus on functional strengthening of children with OI, so an assessment of the muscle contribution to bone injury risk would provide valuable data on the skeletal effects of increased strength and more muscle forces from additional activities such as running, jumping, stairs, etc. Additionally, previous

models did not have OI-specific bone injury limits. Recent work by Albert et al. has provided data on OI bone strength from mechanical testing. This information had been previously inferred from nanoindentation testing results.

The impact of the gluteal muscles on the femoral stresses during simulation of ambulatory loading motivated further examining these muscles during gait analysis in children with OI. Typical clinical gait analysis of children with OI includes EMG assessment for muscle activation timing, but it does not usually include the gluteus maximus or gluteus medius muscles. Due to their impact on femoral stresses, it seemed a necessary next step to analyze their timing during gait in children with OI compared to their age- and gender-matched typically developing peers. During development of the initial femur model, it was anecdotally noted that the modeled OI patient had exhibited prolonged hamstring activity during her clinical gait analysis [14]. This information, though only from one subject, combined with the known sensitivity of the femur to gluteus maximus stresses posed the question of whether the hamstrings may be more active during gait in children with OI in an internal attempt to reduce gluteus maximus use and forces. Both muscles act to extend the hip during stance phase and slow the hip flexion and forward progression of the leg from swing phase. The gluteus medius and gluteus maximus muscles are both accessible with surface EMG electrodes, so this was an easy addition to routine gait analysis procedures. Only activation timing was assessed for this project in order to examine any compensatory or avoidance strategies.

The final project was motivated by the abnormal bone geometry commonly seen in OI. Ideally, patient-specific FE models are generated directly from 3D imaging of the patient, commonly CT scans. However, this imaging modality is not feasible for children

with OI due to its radiation exposure levels. Children with OI are exposed to more medical radiation from x-rays due to their increased fracture rates as well as the common practice of yearly DXA scanning. The original femur model in OI used a standardized femur model [72] and scaled the FE mesh to match the femur size and geometry of a 12-year-old with OI type I based on a coronal plane x-ray [71]. This patient only exhibited mild lateral bowing (5 mm) and a slightly shorter femur than the standardized model. Thus, the geometry fitting was fairly straightforward. The third study of this work aimed to examine if scaling from a single plane image to a 3D model based on normal geometry was an adequate methodology to create an accurate FE model for skeletal stress and strain assessments. One CT of a femur was available from all of the subjects enrolled in the OI study at Shriners Hospitals for Children – Chicago. The available scan was from a 10-year-old female with OI type III who had an intramedullary rod in her right femur and fracture fixation plate across the neck of her left femur. Since the rod could be removed in the image segmentation step, the right femur was used for the analysis. The majority of long bone fractures occur in the diaphysis, so only this region was analyzed. Models developed directly from the CT scan of the children with OI and from a normal, adult femur model scaled to the size of the OI femoral diaphysis were created and analyzed.

5.2. Summary of Findings

The first study tested the hypothesis that increases in femoral maximum principal stress due to a bowing of 30°/15 mm laterally are significantly less than those to a 10% increase in gluteal muscle contractile forces. This hypothesis was accepted and it was found that increasing gluteal forces above their baseline values has a greater impact on the femoral injury risk than does increasing lateral bowing. The results were consistent in

normal pediatric bone, OI type I bone and OI type III bone. Across all bone types, the resultant maximum principal stress values only varied 6 MPa from the mildest simulation (normal bone with no bowing and baseline muscles forces) to the most severe simulation (OI type III bone with 15 mm of lateral bowing and the gluteus medius force increased 20% above baseline). Without knowledge of the yield stress of each bone type, it would be easy to conclude that OI bone is not at greater risk for injury than normal bone. In fact, the normal bone exhibited a higher percent increase in maximum principal stress values with each bowing and muscle force permutation than the OI bone. The models of OI type III had the lowest percent increases in maximum principal stress values. However, using the IR determinant from Equation 2.2, it was demonstrated that these parameters have a potentially detrimental impact on OI bone. Normal pediatric bone had a maximum IR value of 0.38 with a baseline IR of 0.35. The results from OI type I bone showed a baseline IR of 0.66 and a maximum IR of 0.71. OI type III had a maximum IR value of 0.85 with 15 mm of lateral bowing and the gluteus medius force increased by 20% from baseline. The baseline IR value for OI type III bone was 0.79. In OI type III bone, the IR for all bowing levels was lower than the IR for a femur with no bowing, but a gluteus medius increase of only 10% in its force from baseline levels. A similar trend was seen in OI type I bone where the IR value in the models for a 15 mm lateral bowing with baseline muscle forces was the same as the IR value for no lateral bowing and a 10% increase in the gluteus medius muscle force. Throughout all models, the location of the maximum stress values remained in the same area of the lateral side of the femur, just distal to the mid-diaphysis. Orthopaedic management often looks at bone deformity, or level of bowing, to mitigate fracture risk in OI. While this is clearly a factor and a surgical

correction with an intramedullary rod would also provide more support for applied loads, rehabilitative and therapeutic care should also pay attention to the impacts of muscle forces. Variations in activity as well as strengthening exercises can increase the forces produced by the gluteus maximus and gluteus medius muscles [87, 88, 101].

The second study was performed to assess the hypothesis that ambulatory children and young adults with OI type I exhibit significantly different EMG timing patterns than age- and gender-matched controls. Further examination of the activity of the gluteus medius and gluteus maximums muscles during ambulation revealed only one significant difference in timing in children with OI compared to a control population. Thus, the hypothesis was rejected. While not a focus of this study, the children with OI exhibited increased double limb support time and decreased walking speed compared to their peers. The altered gait temporal parameters seen in the OI population may also be a compensatory strategy following fracture healing or as a cautionary strategy from fear of fracturing. The only difference in muscle timing was a delay in gluteus maximus activation onset during the stance phase of gait in the OI population. Only the gluteus medius and gluteus maximus muscles were analyzed for this study, but a prior assessment of a child with OI showed prolonged hamstring activity during the stance phase of gait. These two pieces of information combined may suggest a minimal avoidance strategy to use more hamstring and less gluteus maximus for hip extension. The hamstrings cross the hip and extend the joint, but they do not attach to the femur. No other significant differences were seen in the timing of the gluteus muscles during gait between the two populations, but both populations exhibited timing data that was different from reported normal activation timing [92].

In the final study, the hypothesis femoral stress results from an FE model of a young adult with OI type III are not significantly affected by the clinical imaging modality used to create the patient-specific geometry (patient's CT versus stand 3D model scaled from patient's x-ray) was rejected. The model based on the patient's CT scan exhibited maximum stresses and strains that were twice as high as those obtained from the model based on a normal femur that was scaled to model the OI femur. The CT model and scaled model both had a cortical thickness of approximately 2 mm along their length. The models were the same length of 117 mm and had the same mid-diaphyseal diameter of 14 mm. They had the same material properties and boundary and loading conditions. The differences lied in the smoothness of the geometry and the wider proximal and distal ends of the CT model. The scaled model had a consistent diameter of 14 mm along its entire length. However, the CT model had flaring at its end that widened to a diameter of 48 mm. The models both had their loading applied to a single, centrally located node on the proximal surface of the diaphysis. This meant that the entire load was a compressive force along the diaphysis. The uneven geometry of the CT model meant there were curves in the geometry, which are typical areas of high stress concentrations. The complex geometry of the femur with OI type III may not be compatible with scaling from only a planar image of the bone for creation of an accurate 3D model for FEA.

5.3. Limitations and Future Directions

This work provided valuable data on skeletal loading characteristics in OI while also opening future avenues of exploration. The first study was limited in its OI bone material property data. Each type of bone was assigned material properties based on the three-point bending analysis of specimens from 11-year-old male donors. The available

data was limited to one specimen of an OI type I femur. Though limited, this data is unique and provides the only available information on failure properties of OI bone. A probabilistic statistical analysis would allow for an assessment of how much the variability of material properties would impact the output of the FE models. With a larger data set of properties and yield strengths, the FEA models could represent bounds or the worst case scenarios for assessing bone injury risk during ambulation and other activities. The FE model data set developed in this study could be expanded to include additional levels of lateral bowing, such as 10 mm (20°) which is often a clinical indication for surgical correction to straighten the bone. In addition, other deformities could be modeled. Anterior bowing, long bone torsion, and varying levels of cortical thickness could all be assessed. Other forms of the pathology in the femur that are commonly seen in OI, such as coxa vara, could also be incorporated into the FE modeling options and parameters [102]. Ideally, FE models for assessment of bone injury risk in OI would be patient-specific. However, this is currently not feasible with the available clinical imaging modalities for this population. A larger database of FE models of OI bones would allow more specified models to be created by altering a minimal number of input parameters to assess skeletal loading during a variety of activities beyond gait. One key component to this future assessment opportunity would be the incorporation of musculoskeletal modeling through OpenSim software. Incorporating OpenSim analyses with the first two studies of this work could provide individualized joint loading data from external loading due to ground reaction forces as well as the forces from muscles [103]. Current muscle forces are based on data from normal subjects that was expressed as a percentage of body weight. The differences seen in gluteus maximus activation

timing during the stance phase of gait, diminished walking speed and lower specific force of muscles [94] in children with OI speak to the need to better assess the forces from muscle activation in this population. Although the EMG analysis provided unique data in independently ambulatory children in OI, the study could be expanded and improved. Each population group contained ten subjects; however, the data from two control subjects had to be excluded. Some of the data was highly variable within each group. Prior to comparison between the groups, sides within each group were compared to see if they could be combined. There were no statistical differences between sides in either population. Thus, the control group data was from 14 legs and the OI group data was from 20 legs. The subject ages for this study ranged from 5-17 years of age. This wide age range with the small sample size could account for some of the variability seen in the data. Along with providing more data for better statistical power, a larger population would allow for analysis of differences due to age. A *post-hoc* power analysis of the data revealed that 112 subjects would be needed to detect significant differences in cadence at 80% between the two populations at an alpha level of 0.05. It would also be interesting to study whether age-matching is appropriate in children with OI as they have been shown to sometimes have delayed gait acquisition [96]. Increasing the population size would also provide more data for the OpenSim modeling and, thus, improve the FE models for bone injury assessment in OI.

The final project was mainly limited by the single CT dataset of a femur available in the OI population. The available femur image was from a patient with a severe form of OI. Children with OI type III are at the greatest risk of fracture and could most benefit from accurate predictive models. Future analysis may consider shortening the diaphysis

area being modeled to include only the mid-diaphysis region with a more consistent diameter of 14 mm rather than the fluted ends with a diameter of 48 mm seen in the CT model. Additionally, analyses could be done to examine the effects of the intramedullary rod on the overall strength of the OI bone and the loading distributions. Since both models had no rod and the same material properties, this does not account for the differences seen. Stress concentrations at the interface of the bone and rod may put the OI bone in a weakened state at increased risk of fracture in this region. Stress shielding is a common concern with orthopaedic implants and may be more concerning in OI where the bone strength is much lower than the material strength of metal implants compared to the differences seen in normal bones. The large differences seen in the maximum principal stresses and principal strains make the practice of scaling a normal bone based on a single plane x-ray for FEA a potentially unfeasible practice. It may be necessary to obtain 3D clinical images or a minimum of two x-ray views in order to adequately create representative 3D models of OI bones. The radiation levels of CT scans make this modality an unappealing option. It is possible that MRI scans could be used to obtain patient-specific 3D geometry of OI bone as well as material properties. Further research should be done in this area to determine the feasibility and applicability of this approach. Obtaining material properties directly from a scan of the whole femur would allow an FE model to account not only for the varying cortical thickness and geometry but also for the heterogeneity of the material properties and bone density throughout the entire bone. This would allow FE models to be extremely specified for individuals, but would also provide more general geometry and material data for a database of FE models. A database of

models would allow for patient-tailored models when exact geometry and material properties are not obtainable.

Overall, this project provided valuable data on characteristics seen in OI. Future work should continue to expound on the current knowledge and examine ways to assist orthopaedic and rehabilitative management and treatment of persons with OI. Accurate quantitative data muscle forces and skeletal loading responses may provide clinicians with tools to better assist with therapy and activity prescriptions and restrictions for those with OI. Accurate bone injury risk data may allow children to more fully participate with their peers with less fear of fracture from the activity.

Bibliography

1. Cheung, M.S. and F.H. Glorieux, *Osteogenesis Imperfecta: Update on Presentation and Management*. Reviews in Endocrine & Metabolic Disorders, 2008. **9**: p. 153-160.
2. Harris, G.F., *OI Grant*. 2005, NIDRR: Shriners Hospitals for Children -- Chicago.
3. Shapiro, J.R., *Clinical and Genetic Classification of Osteogenesis Imperfecta and Epidemiology*, in *Osteogenesis Imperfecta: A Translational Approach to Brittle Bone Disease*, J.R. Shapiro, Editor. 2014, Academic Press: Waltham, MA, USA. p. 15-22.
4. Albert, C., J.M. Fritz, and G. Harris, *Biomechanics of Osteogenesis Imperfecta: Current Concepts and Emerging Horizons*, in *Transitional Care in Osteogenesis Imperfecta: Advances in Biology, Technology, and Clinical Practice*, P.A. Smith, F. Rauch, and G.F. Harris, Editors. 2015, Shriners Hospitals for Children -- Chicago: Chicago, IL. p. 27-48.
5. Edwards, W.B. and K.L. Troy, *Simulating distal radius fracture strength using biomechanical tests: a modeling study examining the influence of boundary conditions*. Journal of Biomechanical Engineering, 2011. **133**(11): p. 114301.
6. Edwards, W.B. and K.L. Troy, *Finite element prediction of surface strain and fracture strength at the distal radius*. Medical Engineering & Physics, 2012. **34**(3): p. 290-298.
7. Fritz, J.M., et al., *A fracture risk assessment model of the femur in children with osteogenesis imperfecta (OI) during gait*. Medical Engineering & Physics, 2009. **31**(19): p. 1043-1048.
8. Fritz, J.M., et al., *Muscle force sensitivity of a finite element fracture risk assessment model in osteogenesis imperfecta - biomed 2009*. Biomedical Sciences Instrumentation, 2009. **45**: p. 316-321.
9. Fritz, J.M., et al. *Improved Mesh for a Finite Element Model of Fracture Risk Assessment in Osteogenesis Imperfecta*. in *American Society of Biomechanics Annual Meeting*. 2011. Long Beach, CA.
10. Silience, D.O. and S.R. Lamandé, *Evolution of the Present Understanding of the Clinical and Genetic Heterogeneity and Molecular and Biochemical Basis of Osteogenesis Imperfecta*, in *Osteogenesis Imperfecta: A Translational Approach to Brittle Bone Disease*, J.R. Shapiro, Editor. 2014, Academic Press: Waltham, MA, USA. p. 5-14.
11. Byers, P.H. and R.D. Steiner, *Osteogenesis imperfecta*. Annu Rev Med, 1992. **43**: p. 269-82.

12. Rauch, F., *Osteogenesis Imperfecta Bone on the Tissue Level*, in *Transitional Care in Osteogenesis Imperfecta: Advances in Biology, Technology, and Clinical Practice*, P.A. Smith, F. Rauch, and G.F. Harris, Editors. 2015, Shriners Hospitals for Children -- Chicago: Chicago, IL. p. 135-146.
13. Chabot, G. and L. Zeitlin, *Current Classification, Clinical Manifestations and Diagnostic Issues of Osteogenesis Imperfecta*, in *Interdisciplinary Treatment Approach for Children with Osteogenesis Imperfecta*, R.-M. Chiasson, C. Munns, and L. Zeitlin, Editors. 2004, Shriners Hospitals for Children: Montreal, Canada. p. 1-34.
14. Fritz, J.M., *A Patient-Specific Finite Element Model for Femur Fracture Risk Assessment in Osteogenesis Imperfecta Type I*, in *Biomedical Engineering*. 2007, Marquette University: Milwaukee, WI. p. 82.
15. Zions, L.E. and R.E. Bowen, *Treatment of Fractures and Non-Unions in Children with Osteogenesis Imperfecta*, in *Osteogenesis Imperfecta: A Translational Approach to Brittle Bone Disease*, J.R. Shapiro, Editor. 2014, Academic Press: Waltham, MA, USA. p. 427-442.
16. Albert, C., et al., *Reduced diaphyseal strength associated with high intracortical vascular porosity within long bones of children with Osteogenesis Imperfecta*. *Bone*, 2014. **66**: p. 121-130.
17. Rauch, F., R. Travers, and F.H. Glorieux, *Pamidronate in children with osteogenesis imperfecta: histomorphometric effects of long-term therapy*. *J Clin Endocrinol Metab*, 2006. **91**(2): p. 511-6.
18. Bishop, N.J. and G. Russell, *Bisphosphonates*, in *Osteogenesis Imperfecta: A Translational Approach to Brittle Bone Disease*, J.R. Shapiro, et al., Editors. 2014, Academic Press: Waltham, MA, USA. p. 495-500.
19. Kocher, M.S. and F. Shapiro, *Osteogenesis imperfecta*. *The Journal of the American Academy of Orthopaedic Surgeons*, 1998. **6**(4): p. 225-236.
20. Zeitlin, L., F. Fassier, and F.H. Glorieux, *Modern Approach to Children with Osteogenesis Imperfecta*. *Journal of Pediatric Orthopedics. Part B.*, 2003. **12**(2): p. 77-87.
21. Smith, P., *Femoral bowing correction*, J.M. Fritz, Editor. 2014.
22. Fan, Z., et al., *Mechanical properties of OI type III bone tissue measured by nanoindentation*. *J Biomed Mater Res A*, 2006. **79**(1): p. 71-7.
23. Fan, Z., et al., *Comparison of nanoindentation measurements between osteogenesis imperfecta type III and type IV and between different anatomic locations (femur/tibia versus iliac crest)*. *Connect Tissue Res*, 2007. **48**(2): p. 70-5.

24. Fan, Z.F., et al., *Nanoindentation as a means for distinguishing clinical type of osteogenesis imperfecta*. Composites Part B: Engineering, 2007. **38**(3): p. 411-415.
25. Albert, C., et al., *Bone properties by nanoindentation in mild and severe osteogenesis imperfecta*. Clinical Biomechanics, 2013. **28**(1): p. 110-116.
26. Albert, C.I., J. Jameson, and G. Harris, *Design and validation of bending test method for characterization of miniature pediatric cortical bone specimens*. Proceedings of the Institution of Mechanical Engineers, Part H: Journal of Engineering in Medicine, 2012. **227**(2): p. 105-113.
27. Logan, D.L., *A First Course in the Finite Element Method Using Algorithms*. 2000: Brooks/Cole Publishing Co. 864.
28. Chandrupatla, T.R. and A.D. Belegundu, *Introduction to Finite Elements in Engineering, 3rd Edition*. 2002, Saddle River, NJ: Pearson Education, Inc. 475.
29. Hastings, J., M. Juds, and J. Brauer. *Accuracy and economy of finite element magnetic analysis*. in *33rd Annual National Relay Conference*. 1985.
30. Guo, X., et al., *Critical strain of carbon nanotubes: an atomic-scale finite element study*. Journal of applied mechanics, 2007. **74**(2): p. 347-351.
31. Zavattieri, P.D., *Modeling of crack propagation in thin-walled structures using a cohesive model for shell elements*. Journal of applied mechanics, 2006. **73**(6): p. 948-958.
32. Viceconti, M., et al., *Automatic generation of accurate subject-specific bone finite element models to be used in clinical studies*. Journal of biomechanics, 2004. **37**(10): p. 1597-1605.
33. Brekelmans, W., H. Poort, and T. Slooff, *A new method to analyse the mechanical behaviour of skeletal parts*. Acta Orthop Scand, 1972. **43**(5): p. 301-317.
34. Imai, K., *Computed tomography-based finite element analysis to assess fracture risk and osteoporosis treatment*. World J Exp Med, 2015. **5**(3): p. 182-7.
35. Park, G., et al., *Validation of Shoulder Response of Human Body Finite-Element Model (GHBMC) Under Whole Body Lateral Impact Condition*. Ann Biomed Eng, 2016.
36. Zysset, P.K., et al., *Finite element analysis for prediction of bone strength*. Bonekey Rep, 2013. **2**: p. 386.
37. Kruger, K.M., et al., *Encoding scratch and scrape features for wear modeling of total joint replacements*. Comput Math Methods Med, 2013. **2013**: p. 624267.

38. Kruger, K.M., et al., *Modeling polyethylene wear acceleration due to femoral head dislocation damage*. J Arthroplasty, 2014. **29**(8): p. 1653-1657.e1.
39. Gupta, S., et al., *Development and experimental validation of a three-dimensional finite element model of the human scapula*. Proceedings of the Institution of Mechanical Engineers, Part H: Journal of Engineering in Medicine, 2004. **218**(2): p. 127-142.
40. Edwards, W.B. and K.L. Troy, *Simulating distal radius fracture strength using biomechanical tests: a modeling study examining the influence of boundary conditions*. Journal of biomechanical engineering, 2011. **133**(11): p. 114501.
41. Edwards, W.B. and K.L. Troy, *Finite element prediction of surface strain and fracture strength at the distal radius*. Medical engineering & physics, 2012. **34**(3): p. 290-298.
42. Schileo, E., et al., *Subject-specific finite element models implementing a maximum principal strain criterion are able to estimate failure risk and fracture location on human femurs tested in vitro*. J Biomech, 2008. **41**(2): p. 356-67.
43. Jiang, P., S. Missoum, and Z. Chen, *Fusion of clinical and stochastic finite element data for hip fracture risk prediction*. J Biomech, 2015. **48**(15): p. 4043-52.
44. Väänänen, S.P., et al., *Generation of 3D shape, density, cortical thickness and finite element mesh of proximal femur from a DXA image*. Medical Image Analysis, 2015. **24**(1): p. 125-134.
45. Hambli, R. and S. Allaoui, *A robust 3D finite element simulation of human proximal femur progressive fracture under stance load with experimental validation*. Ann Biomed Eng, 2013. **41**(12): p. 2515-27.
46. Rafferty, B.T., et al., *Design features of a three-dimensional molar crown and related maximum principal stress. A finite element model study*. Dent Mater, 2010. **26**(2): p. 156-63.
47. Albogha, M.H., et al., *Maximum principal strain as a criterion for prediction of orthodontic mini-implants failure in subject-specific finite element models*. Angle Orthod, 2016. **86**(1): p. 24-31.
48. Schileo, E., et al., *To what extent can linear finite element models of human femora predict failure under stance and fall loading configurations?* J Biomech, 2014. **47**(14): p. 3531-8.
49. Keyak, J.H. and S.A. Rossi, *Prediction of femoral fracture load using finite element models: an examination of stress- and strain-based failure theories*. J Biomech, 2000. **33**(2): p. 209-14.

50. Leblanc, A., et al., *Bisphosphonates as a supplement to exercise to protect bone during long-duration spaceflight*. Osteoporos Int, 2013. **24**(7): p. 2105-14.
51. Keyak, J.H., et al., *Effect of finite element model loading condition on fracture risk assessment in men and women: the AGES-Reykjavik study*. Bone, 2013. **57**(1): p. 18-29.
52. Poelert, S., et al., *Patient-specific finite element modeling of bones*. Proc Inst Mech Eng H, 2013. **227**(4): p. 464-78.
53. Taylor, M. and P.J. Prendergast, *Four decades of finite element analysis of orthopaedic devices: Where are we now and what are the opportunities?* Journal of Biomechanics, 2015. **48**(5): p. 767-778.
54. Zadpoor, A.A. and H. Weinans, *Patient-specific bone modeling and analysis: the role of integration and automation in clinical adoption*. J Biomech, 2015. **48**(5): p. 750-60.
55. Varga, P., et al., *Nonlinear quasi-static finite element simulations predict in vitro strength of human proximal femora assessed in a dynamic sideways fall setup*. J Mech Behav Biomed Mater, 2015. **57**: p. 116-127.
56. Schwartz, D., et al., *Development of a computationally efficient full human body finite element model*. Traffic Inj Prev, 2015. **16 Suppl 1**: p. S49-56.
57. Mengoni, M., et al., *Subject-specific multi-validation of a finite element model of ovine cervical functional spinal units*. Journal of Biomechanics.
58. Jackman, T.M., A.M. DelMonaco, and E.F. Morgan, *Accuracy of finite element analyses of CT scans in predictions of vertebral failure patterns under axial compression and anterior flexion*. J Biomech, 2015.
59. Petursson, T., et al., *Bone Mineral Density and Fracture Risk Assessment to Optimize Prosthesis Selection in Total Hip Replacement*. Comput Math Methods Med, 2015. **2015**: p. 162481.
60. Taddei, F., et al., *Mechanical strength of a femoral reconstruction in paediatric oncology: a finite element study*. Proceedings of the Institution of Mechanical Engineers, Part H: Journal of Engineering in Medicine, 2003. **217**(2): p. 111-119.
61. Rees, J.S., *The effect of variation in occlusal loading on the development of abfraction lesions: a finite element study*. Journal of Oral Rehabilitation, 2002. **29**(2): p. 188-193.
62. Matsui, Y., G. Schroeder, and U. Bosch, *Injury pattern and response of human thigh under lateral loading simulating car-pedestrian impact*. 2004, SAE Technical Paper.

63. Schuster, P.J., et al., *Development and validation of a pedestrian lower limb non-linear 3-d finite element model*. Stapp car crash journal, 2000. **44**: p. 315-334.
64. Duda, G.N., et al., *Influence of muscle forces on femoral strain distribution*. Journal of biomechanics, 1998. **31**(9): p. 841-846.
65. Duda, G.N., E. Schneider, and E.Y. Chao, *Internal forces and moments in the femur during walking*. Journal of biomechanics, 1997. **30**(9): p. 933-941.
66. Fritz, J.M., et al., *Muscle force sensitivity of a finite element fracture risk assessment model in osteogenesis imperfecta - biomed 2009*. Biomed Sci Instrum, 2009. **45**: p. 316-21.
67. Lu, T.-W., et al., *Influence of muscle activity on the forces in the femur: an in vivo study*. Journal of Biomechanics, 1997. **30**(11): p. 1101-1106.
68. Polgar, K., et al., *Strain distribution within the human femur due to physiological and simplified loading: finite element analysis using the muscle standardized femur model*. Proceedings of the Institution of Mechanical Engineers, Part H: Journal of Engineering in Medicine, 2003. **217**(3): p. 173-189.
69. Viceconti, M., et al., *The muscle standardized femur: a step forward in the replication of numerical studies in biomechanics*. Proceedings of the Institution of Mechanical Engineers, Part H: Journal of Engineering in Medicine, 2003. **217**(2): p. 105-110.
70. Pomwenger, W., et al., *Need for CT-based bone density modelling in finite element analysis of a shoulder arthroplasty revealed through a novel method for result analysis*. Biomed Tech (Berl), 2014. **59**(5): p. 421-30.
71. Fritz, J.M., et al., *A fracture risk assessment model of the femur in children with osteogenesis imperfecta (OI) during gait*. Medical Engineering & Physics, 2009. **31**(9): p. 1043-8.
72. Viceconti, M., et al., *The standardized femur program*. Journal of Biomechanics, 1996. **29**: p. 1241-1255.
73. Fritz, J., et al. *Improved Mesh for a Finite Element Model of Fracture Risk Assessment in Osteogenesis Imperfecta*. in *35th Annual Meeting of the American Society of Biomechanics*. 2011. Long Beach, CA.
74. Fritz, J.M., et al. *Brittle bone fracture risk with transverse isotropy*. in *37th Annual Meeting of the American Society of Biomechanics*. 2013. Omaha, NE.
75. Caouette, C., et al., *Biomechanical analysis of fracture risk associated with tibia deformity in children with osteogenesis imperfecta: a finite element analysis*. J Musculoskelet Neuronal Interact, 2014. **14**(2): p. 205-212.

76. Fritz, J.M., et al., *Finite Element Modeling and Analysis Applications in Osteogenesis Imperfecta*, in *Transitional Care in Osteogenesis Imperfecta: Advances in Biology, Technology, and Clinical Practice*, P.A. Smith, F. Rauch, and G.F. Harris, Editors. 2015, Shriners Hospitals for Children -- Chicago: Chicago, IL. p. 149-160.
77. Fritz, J.M., et al. *Validation of a Finite Element Model of the Humerus for Fracture Risk Assessment During Assisted Ambulation*. in *39th Annual Meeting of the American Society of Biomechanics*. 2015. Columbus, OH.
78. Slavens, B.A., et al., *An upper extremity inverse dynamics model for pediatric Lofstrand crutch-assisted gait*. *Journal of biomechanics*, 2011. **44**(11): p. 2162-2167.
79. Grover, P., et al., *Mechanical characterization of fourth generation composite humerus*. *Proceedings of the Institution of Mechanical Engineers, Part H: Journal of Engineering in Medicine*, 2011. **225**(12): p. 1169-1176.
80. Orwoll, E.S., et al., *Evaluation of teriparatide treatment in adults with osteogenesis imperfecta*. *The Journal of clinical investigation*, 2014. **124**(2): p. 491.
81. Albert, C., et al., *Material and Structural Aspects of Bone in Osteogenesis Imperfecta*, in *Transitional Care in Osteogenesis Imperfecta: Advances in Biology, Technology, and Clinical Practice*, P.A. Smith, F. Rauch, and G.F. Harris, Editors. 2015, Shriners Hospitals for Children -- Chicago: Chicago, IL. p. 177-194.
82. Schmid, J. and N. Magnenat-Thalmann, *MRI Bone Segmentation Using Deformable Models and Shape Priors*, in *Medical Image Computing and Computer-Assisted Intervention – MICCAI 2008*, D. Metaxas, et al., Editors. 2008, Springer Berlin Heidelberg. p. 119-126.
83. Rauch, F., et al., *Static and dynamic bone histomorphometry in children with osteogenesis imperfecta*. *Bone*, 2000. **26**(6): p. 581-9.
84. Imai, K., *Computed tomography-based finite element analysis to assess fracture risk and osteoporosis treatment*. *World Journal of Experimental Medicine*, 2015. **5**(3): p. 182-187.
85. Graf, A., et al., *Gait characteristics and functional assessment of children with type I osteogenesis imperfecta*. *J Orthop Res*, 2009. **27**(9): p. 1182-90.
86. Albert, C.I., *Mechanical Testing Results from Three-Point Bending of Pediatric Bone Specimens*. 2015.

87. Ellis, R.G., B.J. Sumner, and R. Kram, *Muscle contributions to propulsion and braking during walking and running: insight from external force perturbations*. *Gait Posture*, 2014. **40**(4): p. 594-9.
88. MacAskill, M.J., T.J. Durant, and D.A. Wallace, *Gluteal muscle activity during weightbearing and non-weightbearing exercise*. *Int J Sports Phys Ther*, 2014. **9**(7): p. 907-14.
89. Shin, S.J., T.Y. Kim, and W.G. Yoo, *Effects of various gait speeds on the latissimus dorsi and gluteus maximus muscles associated with the posterior oblique sling system*. *J Phys Ther Sci*, 2013. **25**(11): p. 1391-2.
90. *Plug-in Gait Product Guide -- Foundation Notes*. 2010, Vicon Motion Systems, Ltd. p. 1-76.
91. Di Fabio, R.P., *Reliability of computerized surface electromyography for determining the onset of muscle activity*. *Phys Ther*, 1987. **67**(1): p. 43-8.
92. Perry, J., *Gait Analysis: Normal and Pathological Function*. 1992, Thorofare, NJ: SLACK.
93. Fritz, J.M., et al., *A fracture risk assessment model of the femur in children with osteogenesis imperfecta (OI) during gait*. *Med Eng Phys*, 2009. **31**(9): p. 1043-8.
94. Veilleux, L.-N., et al., *Muscle Anatomy and Dynamic Muscle Function in Osteogenesis Imperfecta Type I*. *The Journal of Clinical Endocrinology & Metabolism*, 2014. **99**: p. E356-E362.
95. Caudill, A., et al., *Ankle strength and functional limitations in children and adolescents with type I osteogenesis imperfecta*. *Pediatr Phys Ther*, 2010. **22**(3): p. 288-95.
96. Brizola, E., A.L. Staub, and T.M. Felix, *Muscle strength, joint range of motion, and gait in children and adolescents with osteogenesis imperfecta*. *Pediatr Phys Ther*, 2014. **26**(2): p. 245-52.
97. Institute, S.C.a.I. *"Seg3D" Volumetric Image Segmentation and Visualization. Scientific Computing and Imaging Institute (SCI)*. Available from: <http://www.seg3d.org>.
98. Shapiro, J.R., et al., *Osteogenesis imperfecta: a translational approach to brittle bone disease*. 2013: Academic Press.
99. Fritz, J.M., et al. *Finite Element Assessment of Pediatric Femoral Response to Loading During Ambulation: Normal vs. Osteogenesis Imperfecta (OI) Bone*. in *39th Annual Meeting of the American Society of Biomechanics*. 2015. Columbus, OH.

100. Shaker, J.L., et al., *Recent developments in osteogenesis imperfecta*. F1000Res, 2015. **4**(F1000 Faculty Rev): p. 681.
101. Jeong, D.E., S.K. Lee, and K. Kim, *Comparison of the activity of the gluteus medius according to the angles of inclination of a treadmill with vertical load*. J Phys Ther Sci, 2014. **26**(2): p. 251-3.
102. Aarabi, M., et al., *High prevalence of coxa vara in patients with severe osteogenesis imperfecta*. J Pediatr Orthop, 2006. **26**(1): p. 24-8.
103. Delp, S.L., et al., *OpenSim: open-source software to create and analyze dynamic simulations of movement*. Biomedical Engineering, IEEE Transactions on, 2007. **54**(11): p. 1940-1950.